Available online at www.sciencedirect.com

ScienceDirect

Advances in Space Research xxx (xxxx) xxx

ADVANCES IN SPACE RESEARCH (a COSPAR publication)

www.elsevier.com/locate/asr

Fast and accurate evaluation of deep-space galactic cosmic ray fluxes with HELMOD-4/CUDA

M.J. Boschini [a,b], G. Cavallotto [a,c], S. Della Torre [a,*], M. Gervasi [a,c], G. La Vacca [a,c,*] P.G. Rancoita [a], M. Tacconi [c]

[a] INFN sez. Milano-Bicocca, Piazza della Scienza, 3, 20126 Milano, Italy
[b] CINECA, Segrate, Milano, Italy
[c] Physics Department, University of Milano-Bicocca, Piazza della Scienza, 3, 20126 Milano, Italy

Received 11 January 2024; received in revised form 15 March 2024; accepted 10 April 2024

Abstract

The accurate knowledge of cosmic ion fluxes is essential for fundamental physics, deep space missions, and exploration activities in the solar system. In the HELMOD-4 model the Parker transport equation is solved using a Monte Carlo approach to evaluate the solar modulation effect on local interstellar spectra of Galactic Cosmic Rays (GCRs). This work presents the latest updates to the HELMOD-4 model parameters, focusing on the descending phase of solar cycle 24. The updates are motivated by the latest high-precision measurements from the AMS-02 detector which revealed for the first time with high accuracy the features of GCR fluxes' evolution during a period of positive interplanetary magnetic field polarity. Furthermore, we present HELMOD-4/CUDA, a GPU-accelerated approach for solving the Parker equation in the heliosphere using a stochastic differential equation method. The code is an evolution of the HELMOD-4 code, porting the algorithm to GPU architecture using the CUDA programming language. This approach achieves significant speedup compared to a CPU implementation. The HELMOD-4/CUDA code has been validated by comparing its results with the most precise and updated experimental GCR spectra observed during high and low solar activity periods, both in the inner and outer heliosphere, at the Earth location, and outside the ecliptic plane. The comparison shows that HELMOD-4 and HELMOD-4/CUDA can be equivalently used to provide solar-modulated spectra with a similar degree of accuracy in reproducing observed data.

Keywords: Solar modulation; Interplanetary space; Cosmic rays; Space weather; Sunspot number; Space radiation environment; Forecast; CUDA; GPU; Stochastic differential equation

1. Introduction

Galactic cosmic rays (GCRs) are high-energy charged particles that originate from outside the solar system. GCRs comprise protons and helium nuclei, with a small fraction of heavier elements. When GCRs enter the heliosphere, which is the region dominated by Sun dynamics, the electromagnetic interaction with the magnetized plasma of the out-flowing wind from the Sun causes a reduction of flux intensity, which is called *solar modulation*. Since solar activity changes on time scales ranging from days to years, and the solar wind and magnetic field vary with time and position in space, the effectiveness of the solar modulation changes with time too, modifying both GCR intensity and spectral shape (for a review see, e.g., Rankin et al., 2022a).

When dealing with the radiation effects on Electrical, Electronic, and Electro-mechanical (EEE) components

* Corresponding authors at: INFN sez. Milano-Bicocca (S. Della Torre) and Physics Department, University of Milano-Bicocca (G. La Vacca), Piazza della Scienza, 3 - 20126 Milano, Italy.
E-mail addresses: stefano.dellatorre@mib.infn.it (S. Della Torre), giuseppe.lavacca@unimib.it (G. La Vacca).

https://doi.org/10.1016/j.asr.2024.04.021
0273-1177/

during space missions, GCRs are extremely dangerous due to their high energies and high rate of energy deposition. They are a significant cause of Single-Event Effects (SEE) in spacecraft electronics, particularly in deep space. Therefore, having an accurate description of the space radiation environment for GCRs through a reliable model of solar modulation is crucial (see, e.g., Golge, 2016; Samwel et al., 2019; Peter et al., 2022; Rahmanian et al., 2023). The accurate characterization of the space radiation environment is also important for fundamental physics studies, where any deviation from the expected behavior of the GCR spectra could be an indication of a new astrophysical signal (see, e.g., Chang et al., 2008; Abdo et al., 2009; Adriani et al., 2009; Cernuda, 2011; Mertsch and Sarkar, 2011; Della Torre et al., 2015; Rozza et al., 2016; Boschini et al., 2021; Boschini et al., 2022d) or exotic physics (see, e.g., Bottino et al., 1998; Cirelli and Cline, 2010; Ibarra et al., 2010; Salati, 2011; Weniger, 2011; Alvey et al., 2023).

Most of our understanding of the transport of GCRs in the heliosphere comes from measurements taken at the Earth's location, *i.e.,* at a distance of 1 astronomical unit (AU, $1\,\mathrm{AU} \simeq 1.5 \times 10^8$ km) from the Sun. These measurements were obtained in the past through detectors flown in the upper atmosphere on balloons (*e.g.,* BESS, Moiseev et al., 1997) or onboard satellites in near-earth space (*e.g.,* PAMELA, Adriani et al., 2011). Among the space missions currently observing GCRs, AMS-02 has been on board the International Space Station (ISS) since May 2011 and has been providing continuous data with unprecedented accuracy for most of GCR nuclei up to $Z = 28$ (*e.g.,* see Aguilar et al., 2021). Deep space missions are rare but are crucial for understanding particle transport in the heliosphere. Ulysses (Simpson et al., 1992; Simpson, 1996; Heber et al., 1996; Ferrando et al., 1996), Voyager 1 and Voyager 2 (Stone et al., 2005; Webber and McDonald, 2013; Richardson et al., 2019) were pioneers in this exploration. They ventured beyond the ecliptic plane and into the far reaches of the heliosphere, providing us with valuable insights. One of their most significant discoveries was a reliable description of the spatial distribution of GCRs. They found a small yet noticeable spatial (*i.e.,* both latitudinal and radial) gradient in GCR intensity in the inner heliosphere, which decreased rapidly with increasing heliocentric distance. This gradient was estimated to be between 1 and 10% per AU, depending on the particle energy and location in the inner heliosphere (*e.g.,* see McDonald et al., 1997; Heber et al., 2008; De Simone et al., 2011; Gieseler and Heber, 2016). For recent reviews on GCR observations and modeling, please refer to Rankin et al. (2022a) and Engelbrecht et al. (2022) and their references.

The HELMOD-4 model[1] is a Monte Carlo code, based on the Parker Transport Equation (PTE, Parker, 1965). It has already shown to be capable of reproducing observed modulated spectra since solar cycle 22 (Bobik et al., 2012; Della Torre et al., 2012; Boschini et al., 2018a; Boschini et al., 2019; Bartocci et al., 2020; Rankin et al., 2022b), with an accuracy level comparable to actual experimental uncertainties (*i.e.,* a few percent for AMS-02 integrated spectra). Additionally, the GALPROP-HELMOD-4 framework (Boschini et al., 2017) has derived the Local Interstellar Spectra (LISs) for particles with the atomic number up to $Z = 28$ (Boschini et al., 2018b; Boschini et al., 2018c; Boschini et al., 2020a; Boschini et al., 2020b; Boschini et al., 2021; Boschini et al., 2022a; Boschini et al., 2022d). As a result, the HELMOD-4 model has shown a greater capability to reproduce high-precision data compared to other solar modulation models commonly used by the space community (Boschini et al., 2022c). The HELMOD-4 model also includes a forecasting tool that can predict GCR fluxes in various locations of the heliosphere for upcoming space missions. The uncertainty of the forecasted cosmic ray intensity is below 15% (at 68% C.L.) for long-time predictions (up to 11 years) (Boschini et al., 2022b). The forecasting tool has also been used to develop the transfer orbit fluence calculator (Boschini et al., 2023), which accurately estimates the space radiation environment due to GCRs along the transfer orbit of space probes traveling in deep space and at the target-specific celestial body.

The present work makes use of recent AMS-02 measurements of daily fluxes for proton (Aguilar et al., 2021), helium (Aguilar et al., 2022), and electron (Aguilar et al., 2023) cosmic rays. With a longer time coverage, these publications expanded and updated previous ones (Aguilar et al., 2018a; Aguilar et al., 2018b) due to improved detector performance, effective acceptance, and understanding of systematic errors. This is the first time that GCR fluxes have been observed with such high accuracy during a period of positive Interplanetary Magnetic Field (IMF) polarity, which is of particular interest to our paper. Our updated HELMOD-4 parameters, which include the latest data releases on solar modulation phenomenology, can be found in Section 2 along with the tuning of the model parameters to the positive polarity periods. In Section 3 we present the GPU implementation of HELMOD-4/CUDA and its performance. We compare simulation results to experimental data and discuss them in Section 4. Finally, we summarize the results of our work in Section 5.

2. Heliospheric propagation of GCR with HELMOD-4

Solar modulation effects can be summarized as a reduction of GCR flux observed in the interplanetary space compared to flux intensities outside the heliosphere (i.e. the Local Interstellar Spectrum, LIS). The particle propagation in the interplanetary medium can be described as a process (discussed in the following) that transforms the LIS (at the heliosphere boundary) to the modulated spectrum observed in the heliosphere. All relevant physical processes involved in solar modulation are included in the Parker

[1] Results presented in this article are available through online calculators at http://www.helmod.org.

Please cite this article as: M. J. Boschini, G. Cavallotto, S. Della Torre et al., Fast and accurate evaluation of deep-space galactic cosmic ray fluxes with HELMOD-4/CUDA, Advances in Space Research, https://doi.org/10.1016/j.asr.2024.04.021

Transport Equation (PTE), named after Eugene Parker who first proposed it in the 1960s (see, e.g. Parker, 1965; Boschini et al., 2019, and references therein):

$$\frac{\partial \mathrm{U}}{\partial t} = \frac{\partial}{\partial x_i}\left(K_{ij}^{S}\frac{\partial \mathrm{U}}{\partial x_j}\right) + \frac{1}{3}\frac{\partial V_{\mathrm{sw},i}}{\partial x_i}\frac{\partial}{\partial T}(\alpha_{\mathrm{rel}} T\mathrm{U}) - \frac{\partial}{\partial x_i}[(V_{\mathrm{sw},i} + v_{d,i})\mathrm{U}], \quad (1)$$

where U is the number density of GCR particles per unit of kinetic energy T (GeV/nucleon), t is time, $V_{\mathrm{sw},i}$ is the solar wind (SW) velocity along the axis x_i, K_{ij}^{S} is the symmetric part of the diffusion tensor, $v_{d,i}$ is the particle magnetic drift velocity (related to the anti-symmetric part of the diffusion tensor), and $\alpha_{\mathrm{rel}} = \frac{T+2m_rc^2}{T+m_rc^2}$, with m_r the particle rest mass per nucleon in units of GeV/nucleon. The terms in the Parker equation describe: (i) the diffusion of GCRs scattered by irregularities of interplanetary magnetic field (IMF), (ii) the adiabatic energy losses/gains due to the propagation in the expanding SW, (iii) an effective convection resulting from the SW advection with velocity $\vec{V}_{\mathrm{sw}}$, and (iv) the magnetic drift effects related to the drift velocity ($\vec{v}_{\mathrm{d}}$). These processes vary according to the intensity level and phase of solar activity, the intensity and polarity of the solar magnetic field, and are rigidity- and charge-sign-dependent.

The HELMOD-4 model solves the Parker equation using the stochastic differential equation (SDE) method in a backward-in-time approach (*e.g.,* see Bobik et al., 2016), taking into account all the mentioned processes, including their proper dependence on particle mass and charge. Therefore, it is reasonable to assume that the same set of parameters used for proton modulation is also suitable for other GCR species. Therefore, the HELMOD-4 model has been employed for protons as well as for all GCR species using the same set of parameters obtained from the tuning to proton data (*e.g.,* see Bobik et al., 2012; Boschini et al., 2018a; Boschini et al., 2019).

As reported earlier, the GALPROP-HELMOD-4 framework was used to derive LISs for GCRs with the atomic number $Z \leq 28$. This was done iteratively by comparing predicted differential fluxes with state-of-the-art GCR measurements from AMS-02 (Aguilar et al., 2021), and other detectors, such as PAMELA (Picozza et al., 2007), ACE/CRIS (George et al., 2009), HEAO-3 (Engelmann et al., 1990), at 1 AU and Voyager (Cummings et al., 2016), outside the heliopause. At present, this framework does not include ultra-heavy GCR ions (*i.e.,* GCRs with Z>28) due to their negligible contribution to the radiation risk evaluation (*e.g.,* SEE rate) in space, particularly when compared to the impact of iron (see A).

2.1. HELMOD-4 parameters

The region of influence of the IMF embedded into the SW is where the modulation occurs. In HELMOD-4 the structure of this region is complex and is based on hydrodynamical considerations (*e.g.,* see Parker, 1963). The heliosphere, to a first approximation, is globally spherical, with a small compression in the nose region which corresponds to the direction where the Sun's relative motion is pointing inside the local bubble. The inner and outer heliosphere are delimited by the termination shock (TS) and the heliopause (HP), respectively. The heliospheric model in HELMOD-4 (Boschini et al., 2019) provides the long-term variation of the distance to TS and HP as a function of time, generally consistent with deep-space spacecraft observations[2].

In HELMOD-4 the component of the symmetric part of the diffusion tensor parallel to IMF ($K_{||}$) is expressed as:

$$K_{||} = \frac{\beta}{3}K_0(P + g_{\mathrm{low}})\left(R_c + \frac{R}{1\mathrm{AU}}\right), \quad (2)$$

where K_0 is the diffusion parameter (see discussion below), β is the particle speed in units of the speed of light, $P = qc/|Z|e$ is the particle rigidity in GV, R is the heliocentric distance from the Sun in AU, and, finally, g_{low} and R_c are parameters tuned to describe radial GCR intensity gradients in the inner heliosphere (see also discussions in Boschini et al., 2019, and reference therein).

The diffusion parameter K_0 introduced in eq. (2) sets the normalization of $K_{||}$, providing the overall contribution of particle flux diffusion to the particle transport in the heliosphere. In HELMOD-4, K_0 varies with time, reflecting the variability of interplanetary medium properties (like the actual solar magnetic field transported by SW and its turbulence) during the different phases of solar cycles. The variability of K_0 was expressed by means of a practical relationship reported in Eq. (6) of Boschini et al. (2018a) as a function of the monthly smoothed sunspot numbers (SSN) and here reported for the sake of convenience:

$$K_0^{SSN} = c_0 + c_1\,\mathrm{SSN} + c_2\,\mathrm{SSN}^2 + c_3\,\mathrm{SSN}^3. \quad (3)$$

Four sets of parameters c_i of eq. (3) were obtained by fitting the K_0 vs. SSN relation for ascending and descending periods with positive and negative IMF polarities. Such a relationship was demonstrated to be adequate for the description of the dependence of the diffusion parameter on solar activity and polarity (*e.g.,* see Bobik et al., 2012; Boschini et al., 2018a; Bobik et al., 2013, and discussions therein).

The current values of K_0 that are being used for the fit were obtained from Eq. (12) in Bobik et al. (2012), which made use of data[3] from Usoskin et al. (2005) and Usoskin et al. (2011) and the SSN (SILSO World Data Center, YYYY; Clette et al., 2015). Both data series have been updated up to the end of 2022. Based on the latest

[2] It has been recently observed that Voyager 2 is currently traveling through the local interstellar medium. This was determined by analyzing the position of HP obtained from the spacecraft's observations (*e.g.,* see discussions in Krimigis et al., 2019; Richardson et al., 2019). To ensure that Voyager 2 remains outside HP from the crossing point to the present date, a practical correction has been made to the HP model in HELMOD-4. The corrected HP position falls within one standard deviation from the averaged HP predicted by the model.

[3] See https://cosmicrays.oulu.fi/phi/phi.html

Please cite this article as: M. J. Boschini, G. Cavallotto, S. Della Torre et al., Fast and accurate evaluation of deep-space galactic cosmic ray fluxes with HELMOD-4/CUDA, Advances in Space Research, https://doi.org/10.1016/j.asr.2024.04.021

available data, which include the minimum of solar activity with positive IMF polarity, the parameters c_i and the root mean square (RMS) values of the relative differences between data and fit were updated and are now reported in Table 1. Note that the c_i parameters for the negative polarity periods can be found in Table 1 of Boschini et al. (2018a) and remain unchanged.

As shown in Fig. 1, the practical relationship (3) provides an overall agreement between calculated diffusion parameters, as a function of SSN, and K_0 values. Moreover, the updated relation allows reducing the correction factor needed to re-scale the absolute value of $K_{||}$ to account for the drift contribution (see discussion in Boschini et al., 2018a). This correction was evaluated using the proton flux during the period of the positive IMF polarity and then applied to both electrons and ions when the condition $qA > 0$ occurs. Here, q is particle charge sign and A is IMF polarity.

The perpendicular diffusion coefficient is assumed to be directly proportional to $K_{||}$, with the ratio of $K_{\perp,i}/K_{||}$ being approximately 0.065 for protons and 0.050 for electrons, for both radial and latitudinal coordinates of the diffusion tensor (Boschini et al., 2018a). As discussed in Bobik et al. (2012), we have used an enhanced $K_{\perp,\theta}$ by a factor of 2 in the polar regions to accurately model the amplitude and rigidity dependence of the latitudinal gradients of GCR differential intensities for protons (see Boschini et al., 2018a, and references therein).

The drift model used in HELMOD-4 was based on the model described in Potgieter and Moraal (1985). It included the description of two types of drift: *regular* drift due to the gradient and the curvature of the heliospheric magnetic field, and the *neutral sheet* drift (described in studies such as Jokipii and Thomas, 1981; Hattingh and Burger, 1995). This model has undergone several modifications and refinements, including the polar correction of the magnetic field, and the suppression factor at rigidities below 1 GV during high-activity periods, as described in Bobik et al. (2013).

The current model includes an additional effective drift suppression tailored for rigidities above 10 GV around solar activity minimum. This suppression was added based on a data-driven approach to ensure that at such energies, diffusion and convection processes dominate the particle propagation in the numerical solution of the Parker equation (Nndanganeni and Potgieter, 2016). The suppression factor for drift velocities is calculated using a logistic function that depends on the particle's rigidity and the solar activity phase. The asymptotic value is one at low rigidities, meaning no suppression occurs. At high rigidities, the asymptotic value is directly proportional to the tilt angle, smoothly ranging between 1 at the solar maximum and as low as 0.1–0.2 at the solar minimum. A constant smoothness parameter regulates the transition between the two regimes, and the transition rigidity is set at 8.5 GV.

2.2. Comparison with observations during the positive IMF period

To update the HELMOD-4 model parametrization, we compared simulation results with the recent AMS-02 proton and electron time-dependent flux measurements. Special attention has been attributed to data interpolation during the descending phase of the positive polarity periods that represents the main result of the present work: the parameters obtained from the accurate and precise AMS-02 measured fluxes were also qualitatively tested with the rates observed in the first 4 years of the Ulysses mission when a similar condition of solar modulation occurred (see Section 4).

The AMS-02 collaboration has recently provided the daily proton (Aguilar et al., 2021) and helium (Aguilar et al., 2022) flux measurements, covering the period from the beginning of the mission up to November 2019. The daily electron fluxes (Aguilar et al., 2023), instead, include the period up to November 2021. The proton and helium fluxes are represented by grey circles in Fig. 2, while the black circles in the same figure represent the daily fluxes grouped in Carrington rotations (CR). For each rigidity bin, the fluxes for each day falling in a particular CR have been averaged using a simple arithmetic mean. The fluxes measured by AMS-02 on the days with solar energetic particles have been excluded from this averaging process.

It's worth noting that during the AMS-02 data-taking period, we observed the ascending phase of the solar cycle with negative polarity, the maximum of the solar activity with polarity change, and the descending phase to the minimum of the solar cycle 24 with positive polarity. This is the first time we have observed the GCR fluxes during the positive IMF polarity period with such high accuracy and precision. Therefore, the extended period allowed for an in-depth adjustment of the balance between the magnetic drift and the diffusion effects at the minimum of the solar activity. As stated in Section 2, the inclusion of explicit magnetic drift suppression was necessary above 10–15 GV to match flux measurements in the latter period. This inclusion ensures that the drift effect gradually subsides with increasing rigidity.

Table 1
Parameters c_i of the polynomial expression (3) for the ascending and descending phase of the positive solar polarity periods. In the last column, the RMS value of the distribution of the relative differences is shown.

	c_0	c_1	c_2	c_3	RMS
A>0 Ascending	0.0002659	−1.24e-6	5.547e−9	−1.343e−11	0.1295
A>0 Descending	0.0002786	−1.65e−6	4.616e−9	−6.590e−12	0.1327

Please cite this article as: M. J. Boschini, G. Cavallotto, S. Della Torre et al., Fast and accurate evaluation of deep-space galactic cosmic ray fluxes with HELMOD-4/CUDA, Advances in Space Research, https://doi.org/10.1016/j.asr.2024.04.021

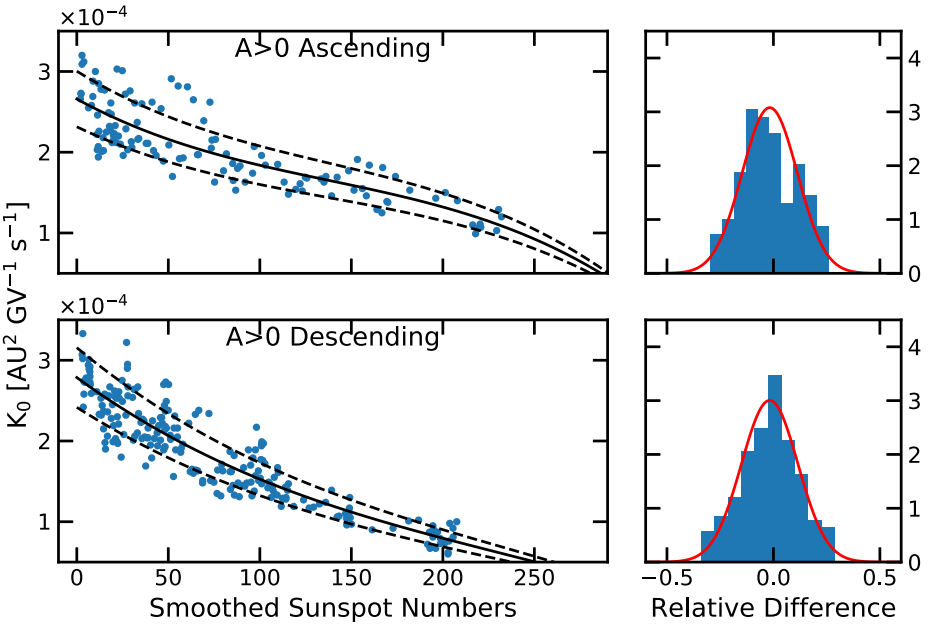

Fig. 1. The diffusion parameter K_0, obtained through the procedure described in Section 2.1 of Bobik et al. (2012), as a function of SSN values (SILSO World Data Center, YYYY; Clette et al., 2015) (blue open points) for the positive polarity period is reported in the left column, during the ascending (upper panel) and descending (lower panel) solar phase. In these panels, the continuous black lines represent the fitted curve to K_0. The dashed lines are obtained by adding (above) or subtracting (below) one standard deviation from the fitted values. The distribution of the relative differences between the data and the fit can be found in the right column. (For interpretation of the references to colour in this figure legend, the reader is referred to the web version of this article.)

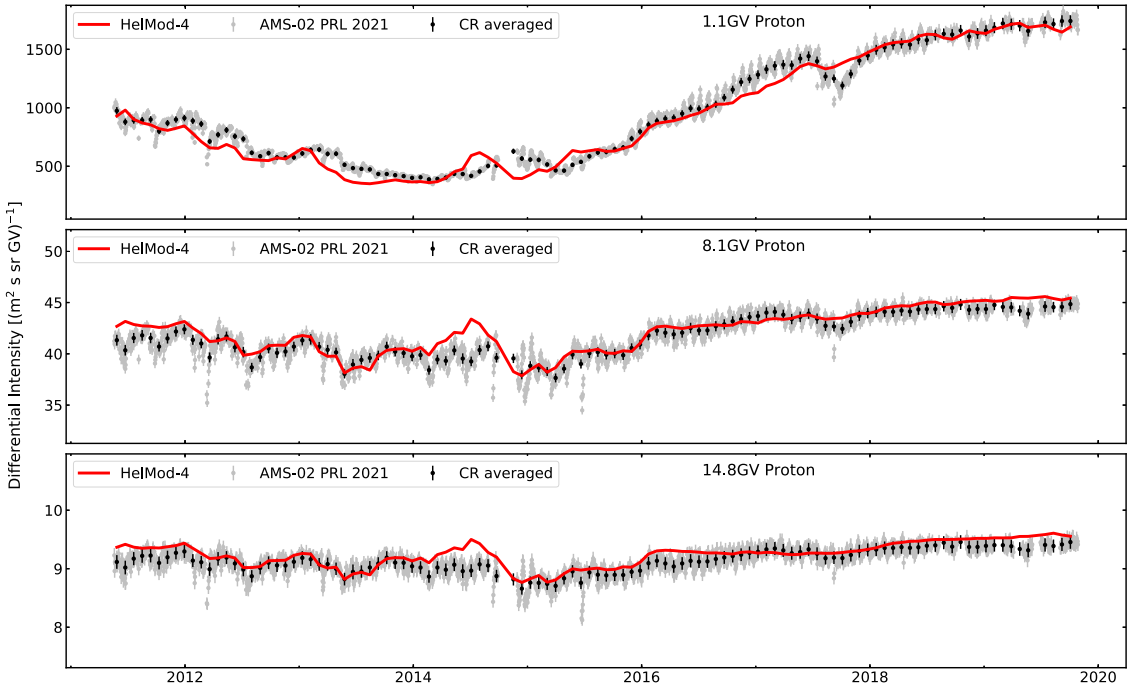

Fig. 2. Solutions of HELMOD-4 for protons at three different rigidities are reported in the panels as solid red lines. The gray dots indicate daily fluxes from AMS-02, while the black dots represent their averages in CR time intervals.

Please cite this article as: M. J. Boschini, G. Cavallotto, S. Della Torre et al., Fast and accurate evaluation of deep-space galactic cosmic ray fluxes with HELMOD-4/CUDA, Advances in Space Research, https://doi.org/10.1016/j.asr.2024.04.021

Furthermore, these data sets update and extend those presented in the previous publications which reported p and He (Aguilar et al., 2018a), and electron (Aguilar et al., 2018b) fluxes on the timescale of Bartels rotations (BR: 27 days) up to May 2017. The agreement of the p dataset in Aguilar et al. (2018a) and the one in Aguilar et al. (2021) results better than two sigmas when fluxes are averaged over the overlapping period. Therefore, considering the sensitivity of the model, slight adjustments in the HELMOD-4 parameters for the periods before May 2017 are necessary to ensure a general good agreement with the latest p dataset.

The outcome of the parameter tuning is shown in Fig. 2, where the simulation results from HELMOD-4 are shown as red lines. Both data and simulations are shown at rigidities 1.1, 8.1, and 14.8 GV, corresponding to the center of selected rigidity bins.

3. The GPU-accelerated model

The PTE, discussed in Section 2, describes the particle's transport through the heliosphere. Nowadays it has become of common use in the scientific community to solve PTE numerically employing the Monte Carlo integration of an equivalent set of stochastic differential equations (SDE, see Section 3.1 and, e.g., Florinski and Pogorelov, 2009; Effenberger et al., 2012; Kopp et al., 2012; Zhao et al., 2014; Boschini et al., 2019; Moloto et al., 2019; Vogt et al., 2020). The integration algorithm structure of SDE is very suitable for parallel computing, particularly GPU architectures. This property allows the possibility to design accelerated algorithms and then to increase the performances of the computation (see, e.g., Dunzlaff et al., 2015; Vogt et al., 2020; Solanik et al., 2021; Solanik et al., 2023). In fact, the integration of PTE is done along stochastic paths, that are independent. The ensemble of all simulated realizations –*i.e.,* the integrals of each stochastic path that can be computed separately by a dedicated thread– would allow one to calculate the solution of the equation. In this field, the use of GPUs for this purpose represents a huge speedup in computing the GCR solar modulation, opening the feasibility of additional studies that need a large number of simulations and the systematical application to the assessment of space radiation effects considering those cases like deep-space missions for which GCRs are largely contributing to hazard. In fact, assessing the GCR contribution to the space radiation environment is a complex operation due to the time variability of GCR flux. Physically motivated models like HELMOD-4 are key tools used to describe the transport of particles through the interplanetary medium. These methods have been used up to now only by specialists due to the long computational effort needed. Now, thanks to GPU algorithms like the one presented in this paper, these models will surely become achievable by general-purpose users.

In this section, we present the GPU-accelerated algorithm applied to the HELMOD-4 model along with the performance gained in comparison with the use of a CPU algorithm without any parallel optimization.

3.1. Stochastic Integration

Solving the PTE is challenging due to the nonlinear nature of the equation and the complexity of the interplanetary medium. There are typically three approaches: the calculation of exact solutions of eq. (1) under specific approximations (see, e.g., Kolesnyk et al., 2020), the numerical integration of the discrete equation using a finite differences or finite elements integration method (see, e.g., Corti et al., 2019; Shen et al., 2019; Ngobeni et al., 2020), and the use of Monte Carlo integration technique that solves an equivalent set of SDEs (see, e.g., Florinski and Pogorelov, 2009; Effenberger et al., 2012; Kopp et al., 2012; Zhao et al., 2014; Boschini et al., 2019; Moloto et al., 2019; Vogt et al., 2020; Solanik et al., 2023). The equivalence between PTE and SDE can be demonstrated using the so-called "Ito's formula" as shown in Section 4. 3.2–4.3.5 of Gardiner (1985). The diffusion process is a particular class of Markov processes and, thus, can be described by a *Fokker–Planck equation*[4] (Eq. 1.7.15 in Klöden and Platen, 1999) and by a set of SDEs as well (see, e.g., Chapter 1.6–1.7 of Klöden and Platen, 1999).

Using this approach the problem is reduced to finding a solution of the stochastic integral of a set of ordinary differential equations instead of the integral of a partial derivative differential equation. The use of an SDE-based numerical scheme leads to numerous advantages with respect to other numerical methods. As pointed out by Strauss and Effenberger (2017) these can be summarized as i) unconditional stability (although this does not necessarily imply numerical accuracy), ii) the method can handle large gradients, iii) it allows saving computational memory, and, last but not least, iv) it can be performed on parallel computational environments (see Strauss and Effenberger, 2017, for a complete overview of the use of SDE in particle transport problem in heliosphere).

To obtain the SDEs equivalent to Eq. (1), the latter should be rewritten to match the following formulation (see e.g. Eq. 13 of Zhang (1999), Equation A2 of Strauss et al. (2011), Eq. 14 of Kopp et al. (2012)):

$$\frac{\partial Q}{\partial s} = \sum_i A_i(s,y)\frac{\partial Q}{\partial y_i} + \frac{1}{2}\sum_{i,j} C_{ij}(s,y)\frac{\partial^2 Q}{\partial y_i \partial y_j} - LQ + S \qquad (4)$$

where Q is the generic transition density function with respect to the initial state in a phase-space point y at time s, A_i is the advective term for $i-th$ coordinate (e.g. convection due to solar wind and magnetic drift), $\boldsymbol{C}$ is the diffusion tensor, L describes (catastrophic) "losses" and finally S describes "source" of particles; in this formulation

[4] Please note that this name is usually referred to the forward-in-time formulation, while backward-in-time formulation, instead, is usually referred as Kolmogorov backward equation.

Please cite this article as: M. J. Boschini, G. Cavallotto, S. Della Torre et al., Fast and accurate evaluation of deep-space galactic cosmic ray fluxes with HELMOD-4/CUDA, Advances in Space Research, https://doi.org/10.1016/j.asr.2024.04.021

$\partial s > 0$ represents a propagation backward-in-time. The Stochastic approach allows re-evaluating the diffusion process in Eq. (4) employing a set of SDEs that can be generally expressed for the backward-in-time evolution as:

$$dy_i(s) = A_i ds + B_{i,j} dW_j(s), \tag{5}$$

where $\boldsymbol{C} = \boldsymbol{B}\boldsymbol{B}^T, d\vec{W}$ represents the increments of a *standard Wiener process* that can be depicted as an independent random variable of the form $\sqrt{ds}N(0,1)$ and, finally, $N(0,1)$ denotes a normally distributed random variable with zero average value and unit variance (see e.g., Appendix A of Zhang (1999) and Section 2 of Higham (2001)). Further information about SDEs solved in the HELMOD-4 model, and their derivation, could be found in Bobik et al. (2016, 2018a).

3.2. GPU implementation

Among the numerical algorithms available to integrate SDEs, the most simple to be implemented follows the well-known Euler-Maruyana scheme (see, e.g., Kroese et al., 2011, Section 5.6.1) in combination with the Ito rule (see discussion in Bobik et al., 2016, and reference therein). The Ito stochastic integral evaluates SDE coeffcients at the pre-point, i.e., one of the borders of the integration step. A more appropriate choice would be to use the Stratonovich integral (where SDE coeffcients are evaluated at the midpoint of the integration step) because the midpoint is close to the actual time when random forces are applied. Unfortunately, this kind of numerical integration has mathematical properties which are difficult to handle in numerical codes and, thus, the Ito approach is usually preferred (see, e.g., discussion in Zhang, 1999).

In the numerical integration algorithm, the temporal evolution of an ensemble of real particles (or, equivalently, the evolution of a *phase–space density element*) defined by eq. (1) can be described by means of a computational structure that is usually referred as *quasi-particle object* (or *pseudo-particle object*)[5]. We follow the backward-in-time approach in which the simulation starts from a specific position in the heliosphere, which represents a hypothetical observer (like, e.g., a particle detector or a deep-space probe), and evolves the quasi-particle objects back in time, i.e. gaining energy (momentum) moving towards the heliosphere boundary, in an inward directed solar wind. At the end of the backward propagation, the quasi-particle objects contribute to the final spectra with a weight related to the LIS at the final energy which is proportional to the *loss* term in eq. (4) (see Eq. 22 in Bobik et al., 2016):

$$J_{mod}(T_{initial}) \propto \sum_{k=1}^{N} LIS(T_{bound,k}) \cdot \exp\left(-\sum_{j=0}^{m} L_{B,j} \cdot \Delta s\right) \tag{6}$$

where $J_{mod}(T_{initial})$ is the modulated spectra at energy $T_{initial}$, $\mathcal{N}$ is the number of simulated quasi-particle objects with initial energy $T_{initial}$, $T_{bound,k}$ is the quasi-particle objects energy at heliosphere boundary, m is the number of integration steps from the origin to the boundary, $L_{B,j}$ is the *loss* term in eq. (4) evaluated at step j, and Δs is the integration time step.

From the point of view of the algorithm, the same operation, i.e. evaluating eq. (5), is performed across multiple data elements simultaneously as described by the SIMD paradigm (single instruction, multiple data, as opposed to SISD, i.e. single instruction single data, corresponding to the traditional von Neumann architecture, *e.g.,* see Cheng et al., 2014) which is optimal for GPU architecture. In the HELMOD-4/CUDA we rewrote the original algorithm of HELMOD-4 using CUDA-C language[6] to optimize the architecture for NVIDIA-Ampere hardware. In the present approach, the evolution of *quasi-particle* objects is assigned to different GPU threads. In the case of multiple GPUs, the algorithm assigns to each GPU a subset of energies to be simulated; within this approach, it is not needed to share memory across devices and each CPU thread can proceed independently from the others; in the final step, the final histograms only are transferred to the host without the need of further merging. A key point in the code development is the choice of the pseudo-random number generators (PRNGs, Askar et al., 2021). In this implementation, we used the *Philox4_32_10* generator (Salmon et al., 2011) provided by the device API of the cuRAND library to generate per-thread random numbers within *quasi-particle* propagation kernel. The PRNG is initialized by using the same seed for each kernel call on the same GPU but specifying a different sequence identifier related to the id of the thread (see, e.g., PRNG implementation in Romero et al., 2020). This generator is a counter-based PRNG that uses a cryptographic technique to produce high-quality statistical independence random numbers with a very fast and lightweight algorithm (see, e.g., discussion in Askar et al., 2021).

The algorithm was optimized to compute the average differential intensity along a designed orbit for deep space missions. This is done by distributing the total set of *quasi-particles* objects into subsets each one referring to the different initial positions and heliospheric parameters. Once all subsets have the same statistics, the final solution, i.e. the weighted distribution of energy at the heliosphere boundary for each initial energy, is equivalent to that obtained by performing separate Monte Carlo realizations for each CR and averaging the results. Finally, we ensure that each warp, which is the minimum GPU synchronous hardware unit executing code instructions in parallel,

[5] This definition is commonly used because it draws a parallel between stochastic propagation and deterministic real particle motion. However, this analogy is figurative and not entirely appropriate as the SDE solution is probabilistic. As pointed out by Strauss and Effenberger (2017), one has to remember that integrating eq. (5) for a single *quasi-particle* has no significance, as integration must be carried out over a large number of possible independent trajectories to define the solution for eq. (1).

[6] https://developer.nvidia.com/cuda-toolkit

evolves *quasi-particles* objects of the same subset to maximize the probability of broadcast data from device memory. Thus, the total amount $\mathcal{N}$ of simulated *quasi-particles* objects is adjusted to be a multiple of the size of a *warp*, i.e. 32 for NVIDIA GPUs with *Compute Capability* version 8.0, this also maximizing the GPU occupancy.

3.3. Algorithm validation

To validate HELMOD-4/CUDA we compared the numerical result with those obtained by HELMOD-4 on CPU architecture. In Fig. 3 we show modulated spectra of proton and carbon GCR measured by AMS-02 (Aguilar et al., 2021) along with the differential intensities computed by HELMOD-4 and HELMOD-4/CUDA for the same period. The second and third panels of Fig. 3 report the relative difference of simulations from experimental data. From this figure, it is hard to distinguish results coming from the two algorithms. Differences are consistent with the uncertainties due to simulated statistics in the Monte Carlo solvers. The same comparison was performed, providing similar results, with all the experimental datasets used to validate HELMOD-4 model within the HelMod-GALPROP framework (i.e. the intensities reported in Boschini et al., 2017; Boschini et al., 2018b; Boschini et al., 2020a; Boschini et al., 2020b; Boschini et al., 2021; Boschini et al., 2022a; Boschini et al., 2022d).

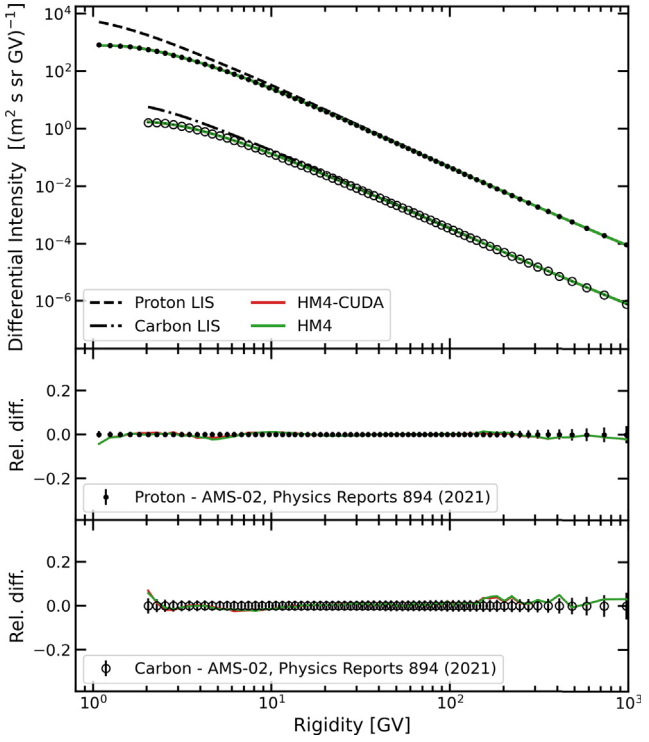

Fig. 3. Top panel: Modulated differential intensity of GCR proton and carbon spectra as obtained from HELMOD-4 (green) and HELMOD-4/CUDA (red) for the integrated period 2011–2018. Dashed and dot-dashed lines represent, respectively, the proton and the carbon LIS as defined in Boschini et al. (2020b). Black points and empty circles represent, respectively, proton and carbon spectra as measured by AMS-02 and reported in Aguilar et al. (2021). The color code is the same in the other panels of this figure. Middle (Bottom) Panel: Relative difference of HELMOD-4 (HM4) and HELMOD-4/CUDA (HM4-CUDA) modulated spectra with AMS-02 protons (carbon) observations, whose relative uncertainties are reported in black, for the same time interval. In all panels, red and green curves almost overlapped since the differences between HM4 and HM4-CUDA are below a few percent and experimental uncertainties. (For interpretation of the references to colour in this figure legend, the reader is referred to the web version of this article.)

For a more general comparison, we considered the period 2020–2046 and the energy range from ~ 0.1 to ~ 20 GeV/n. This period covers a complete solar cycle in both polarities and considers the two typical usages of HELMOD-4: reproducing past measurements and forecasting GCR intensities for future space missions (see, Boschini et al., 2022b, for a discussion on how the forecast is implemented in HELMOD-4). Each simulation was compared bin-by-bin to compute the relative difference of HELMOD-4/CUDA results with respect to the HELMOD-4 ones (see Fig. 4-left). For each bin, the mean relative difference and the standard deviation were computed. As reported in Fig. 4-right, representative of a typical result, the relative differences are distributed normally around zero. This means that the new algorithm does not introduce a significant systematic difference from the CPU one. The results of this comparison, for all energy bins, are summarized in Fig. 4-left for four of the most abundant GCR species (proton, carbon, silicon, and iron). All the other ions behave similarly. The horizontal dashed black line in Fig. 4-left marks the $\sim 2\%$ uncertainties level, which was computed using the uncertainty propagation formula, assuming that each simulation has an intrinsic Poisson distributed uncertainty due to the number of simulated *quasi-particle* objects (i.e. $\mathcal{N} = 5'024$). The fact that the relative difference between the two algorithms is well confined within these bands is proof of the equivalence of the Monte Carlo solvers, *i.e.,* as further discussed in Sections 3.4 and 3.5, HELMOD-4 and HELMOD-4/CUDA can be equivalently used to provide solar-modulated spectra with a similar degree of accuracy in reproducing observed data. In fact, a more precise discussion should take into account that, as shown in the next section, Poisson-like uncertainties can be considered as a very conservative estimation of the uncertainties for this Monte Carlo method, especially for energies greater than 1 GeV/n; nevertheless, similar conclusions arise by using the uncertainties computed in Section 3.5.

3.4. Code performances

The main motivation for developing a GPU-accelerated algorithm is the boost in performance. In this section, we show the performance of HELMOD-4/CUDA algorithm with respect to HELMOD-4 (*i.e.,* the CPU code version) using the same parameters. HELMOD-4 was executed on a server with two CPU Intel(R) Xeon(R) 2.10 GHz. Since the algorithm used by HELMOD-4 does not use any software parallelization

Please cite this article as: M. J. Boschini, G. Cavallotto, S. Della Torre et al., Fast and accurate evaluation of deep-space galactic cosmic ray fluxes with HELMOD-4/CUDA, Advances in Space Research, https://doi.org/10.1016/j.asr.2024.04.021

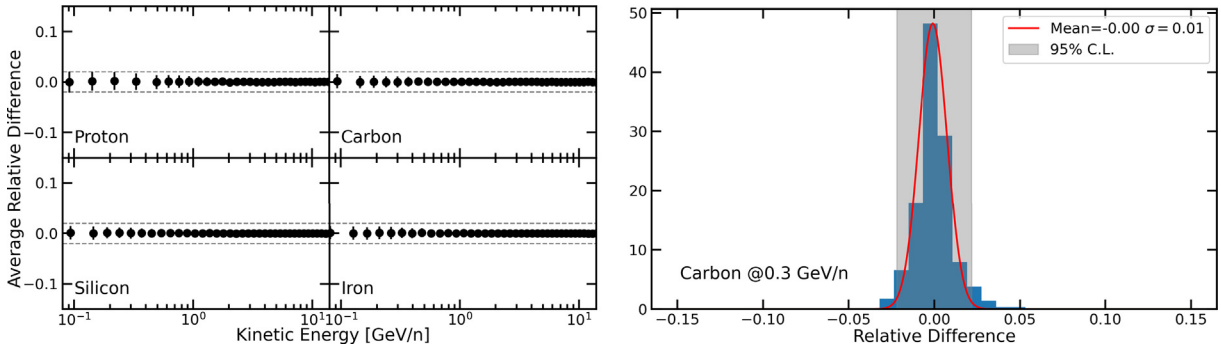

Fig. 4. Relative difference of HELMOD-4/CUDA results with respect the HELMOD-4 ones. The left panel summarizes the mean relative differences computed for each bin in the time interval from 2020 to 2046. The values are computed for proton-, carbon-, silicon- and iron-modulated spectra. The horizontal dashed black lines mark the $\sim 2\%$ uncertainty level. The right panel reports an example of how each point in the left panel is computed: for each energy bin we evaluated the distribution of the relative differences of the algorithms in the time interval 2020–2046 for each Carrington rotation. Then, the mean and standard deviation are computed. In this plot, we superimposed a Gaussian fit and the grey band represents the 2-σ uncertainty.

technique (i.e. each program uses one CPU-core), we recursively execute at the same time 30 HELMOD-4 instances in order to not saturate the CPU resources. HELMOD-4/CUDA was executed on the same server with two GPU NVIDIA A30[7]. Although HELMOD-4/CUDA was designed to use all GPUs available, for these tests we forced the code to use only one GPU, allowing it to execute at the same time 2 HELMOD-4/CUDA instances. Moreover, the code was compiled with the compilation flag `--use_fast_math` which would result in lower numerical accuracy but with a huge improvement in reducing the run time. To evaluate the code performances under different working conditions, we computed the execution time of several energy bins and with a different number of *quasi-particle* objects from $\mathcal{N} = 10^2$ to 10^5. This measurement is obtained by averaging over ~ 200 HelMod instances. In this study, we considered 3 different Carrington rotations (i.e. CR numbers CR-1937, CR-2091, and CR-2132) corresponding to two consecutive solar minima (with opposite solar polarity) and a solar maximum period. The results among the three different periods are qualitatively similar, producing the same relative dependence from $\mathcal{N}$ but with different absolute normalization due to the different modulation parameters. In Fig. 5 the execution time in minutes of the two algorithms is shown as a function of $\mathcal{N}$. Due to the linearity of the algorithm, the execution time of HELMOD-4 scales as a power law of $\mathcal{N}$ with spectral index 1, i.e. a linear function. On the other hand, the execution time of HELMOD-4/CUDA shows two different regimes: up to $\mathcal{N} \sim 10^4$ it scales as a power law with spectral index ~ 0.1, then the spectral index become steeper. This is because at $\mathcal{N} \sim 10^4$ the program saturated the GPU resources and additional operations are required. At $\mathcal{N} \sim 10^5$ we also register sporadic *illegal memory errors*. The observed performances represent a huge improvement with respect to the initial HELMOD-4 code. In Fig. 6 we reported the improving

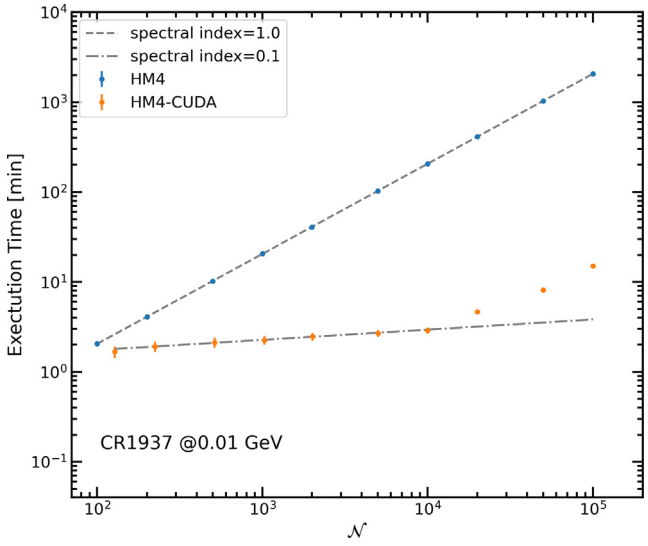

Fig. 5. HELMOD-4(blue points) and HELMOD-4/CUDA(orange points) execution time in minutes with respect to the number of simulated events $\mathcal{N}$ for the case of 0.01 GeV GCR protons at Earth orbit on CR-1937. The grey lines represent the linear fit of the point in the $\mathcal{N}$-range $10^2 \sim 10^4$. HELMOD-4/CUDA execution times are evaluated by using 1 GPU board. (For interpretation of the references to colour in this figure legend, the reader is referred to the web version of this article.)

speed-up factor evaluated as the ratio between HELMOD-4 and HELMOD-4/CUDA execution time for proton GCR during the CR-1937 for several kinetic energy. The results for CR-2091 and CR-2132 are similar and confirm an average improving factor of ~ 40 in run speed-up for the case of $\mathcal{N} \sim 5$/000. One has to note that a similar improvement factor could be obtained also by a proper CPU paralleling algorithm, using all the available CPU cores. Anyway, the availability of high-performance GPUs at affordable cost makes the GPU solution very competitive. In addition, the possibility to install several GPUs on a relatively small cluster, if compared with a configuration hosting the same number of CPU cores, makes this solution also much more reliable in terms of requested room, power, and services. At

[7] https://www.nvidia.com/en-us/data-center/products/a30-gpu/

Please cite this article as: M. J. Boschini, G. Cavallotto, S. Della Torre et al., Fast and accurate evaluation of deep-space galactic cosmic ray fluxes with HELMOD-4/CUDA, Advances in Space Research, https://doi.org/10.1016/j.asr.2024.04.021

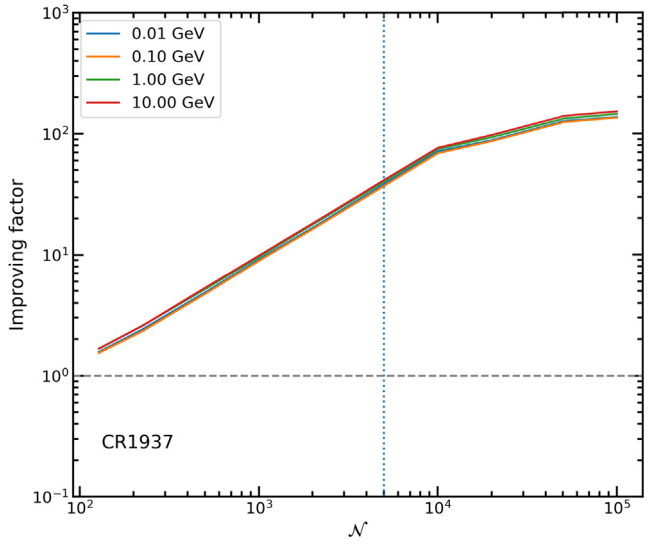

Fig. 6. Improving factor in processing speed by using GPU algorithm with respect to the CPU one. Simulations are performed for GCR protons at Earth orbit on CR-1937 and for four different initial energies. The factor is computed by the ratio of points in Fig. 5 interpolated to match the same $\mathcal{N}$-value.

the time of this publication, the A30 board, developed in 2020, does not represent anymore the state-of-art of GPU hardware[8], thus better performances are expected on new generation devices with the *Hopper* architecture.

3.5. Numerical uncertainties

An interesting application of the GPU-accelerated algorithm is the evaluation of the numerical uncertainties contribution to the total model uncertainty. This kind of calculation requires a huge amount of Monte Carlo realizations to study the statistical properties of the numerical solutions. The new algorithm developed for HELMOD-4/CUDA allows one to scale down to a local GPU farm the computing effort that otherwise would require a large HPC cluster.

The assessment of the numerical uncertainties due to the numerical method itself is an important topic that directly impacts the model uncertainties. Having control of such sources of uncertainty could allow one to disentangle numerical artifacts from the physical model under study. For example, Mykhailenko and Bobik (2022) showed the dependence of the statistical error in the case of the 1D-SDE Monte Carlo model. They found an empirical relationship as a function of initial energy, to calculate the value of $\mathcal{N}$ which sets the numerical uncertainty of the computed flux at 1%. Following a similar approach, we studied the Monte Carlo uncertainties for the 2D-SDE HELMOD-4/CUDA model due to the finite number of *quasi-particles* objects simulated. We considered the three Carrington rotations studied in Section 3.4 (i.e. CR numbers CR-1937, CR-2091, and CR-2132). For the three cases, we generated 200 HELMOD-4/CUDA simulations for various energies with different statistics. For each energy bin, we computed the mean simulated fluxes and the corresponding standard deviation ($\sigma_{r,sim}$) which is then compared with the Poisson relative uncertainty (i.e. $\sigma_{r,pois} = \mathcal{N}^{-\frac{1}{2}}$).

In Fig. 7 we show the uncertainty ratio $\frac{\sigma_{r,sim}}{\sigma_{r,pois}}$ as a function of proton kinetic energy. Each point is averaged among ten realizations evaluated with $\mathcal{N}$ in the range $10^2 \sim 10^5$. We found that this ratio does not depend on the number of realizations (this is also in agreement with what was founded in Mykhailenko and Bobik, 2022). Therefore, this averaging is fully justified. The uncertainty ratio for the three periods is different, so we attempt to provide a *safety threshold* that assesses a value of $\mathcal{N}$ in order to set the numerical uncertainty of the computed flux below $\sigma_{r,sim}$. Thus, we interpolated the uncertainty ratios ($\frac{\sigma_{r,sim}}{\sigma_{r,pois}}$) with the function:

$$f_{unc} = \frac{aT^b}{T^c + d} \tag{7}$$

we pick the largest f_{unc} among the three. Then we define the *safety threshold* as two times the value $\mathcal{N}$ defined from f_{unc} so that:

$$\mathcal{N}_{\text{SafetyThreshold}} = 2 \cdot \sigma^2_{r,sim} \cdot \left(\frac{T^c + d}{a \cdot T^b}\right)^2 \tag{8}$$

where $a = 1.29 \pm 0.07, b = -0.85 \pm 0.01, c = -0.85 \pm 0.01$, and $d = 1.5 \pm 0.1$. It is worth noticing that at low energies

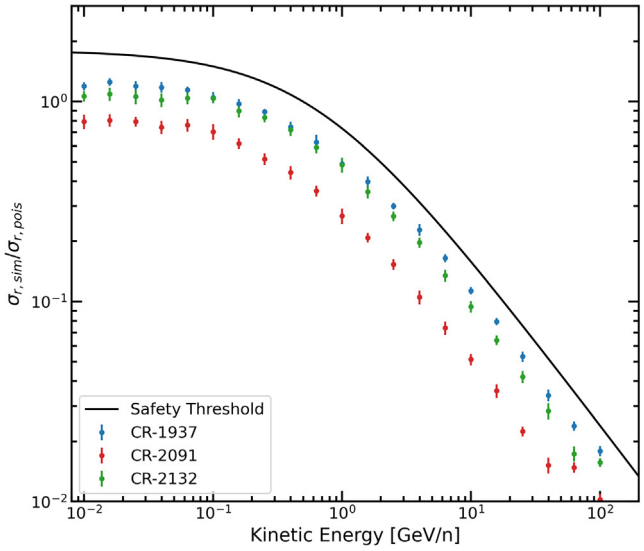

Fig. 7. Uncertainty ratio $\frac{\sigma_{r,sim}}{\sigma_{r,pois}}$ as a function of proton kinetic energy evaluated for CR-1937 (blue points), CR-2091 (red-points) and CR-2132 (green points). Each point is averaged among ten realizations evaluated with $\mathcal{N}$ in the range $10^2 \sim 10^5$. the black line represents the *Safety Threshold* considered to evaluate Eq. (8). (For interpretation of the references to colour in this figure legend, the reader is referred to the web version of this article.)

[8] *e.g.*, for HELMOD-4/CUDA performances using A100 see Della Torre et al. (2023)

(i.e. below ~ 0.1 GeV/n) the numerical uncertainty of simulations is compatible with Poisson statistics, while for larger energies the uncertainties on the results rapidly decrease down to very low levels. We found that energy greater than 10 GeV/n precise results (i.e. $\sigma_{r,sim} < 1\%$) can be achieved with $\mathcal{N} \lesssim 200$. Besides, it is important to remark that the correct numerical uncertainties should be evaluated case by case. Nevertheless, the *Safety Threshold* presented here should be considered as a rough estimation of the numerical uncertainties upper limit due to the 2D-SDE Monte Carlo method and it is intended to give an initial (and safe) value of $\mathcal{N}$.

4. Discussion

To verify the consistency of the updated parametrization with the previous observations, the HELMOD-4 model results have been compared with measurements of proton and electron fluxes throughout two solar cycles and more. These measurements were taken at 1 AU and at greater distances from the Sun, up to the edge of the heliosphere, and outside of the ecliptic plane.

In the following, the comparison of simulation results for proton, electron, and selected GCR ions with flux measurements in various locations of the heliosphere and various time resolutions are shown.

4.1. GCR fluxes at 1 AU

In Fig. 8, various data sets for proton, helium, and electron cosmic ray fluxes at 1 AU, at the lowest rigidity bin in common (*i.e.,* around 2 GV), together with HELMOD-4/CUDA simulation results (red lines) are shown. Besides the AMS-02 measurement already discussed in Section 2.2, PAMELA measurements were also included. The proton (Adriani et al., 2013; Martucci et al., 2018) and helium (Marcelli et al., 2020; Marcelli et al., 2022) flux measurements by PAMELA cover the minimum of solar activity in negative polarity from mid-2006 up to the maximum in mid-2014. The measurements were taken at various time intervals, ranging from monthly to multi-month based, and they overlap in time with the initial part of the AMS-02 data-taking period. The PAMELA electron flux measurements (Adriani et al., 2015) cover only the descending phase of the solar cycle, up to the end of 2009. Additionally, yearly proton fluxes from 1995 to 2014 by SOHO/EPHIN (Kühl et al., 2017) and BESS from 1997 to 2007 (*e.g.,* see Shikaze et al., 2007; Haino et al., 2004; Abe et al., 2016) were included to complete the selected database.

Despite the various levels of accuracy in the data from the different experiments, a general agreement between the data and simulations can be observed in Fig. 8. When

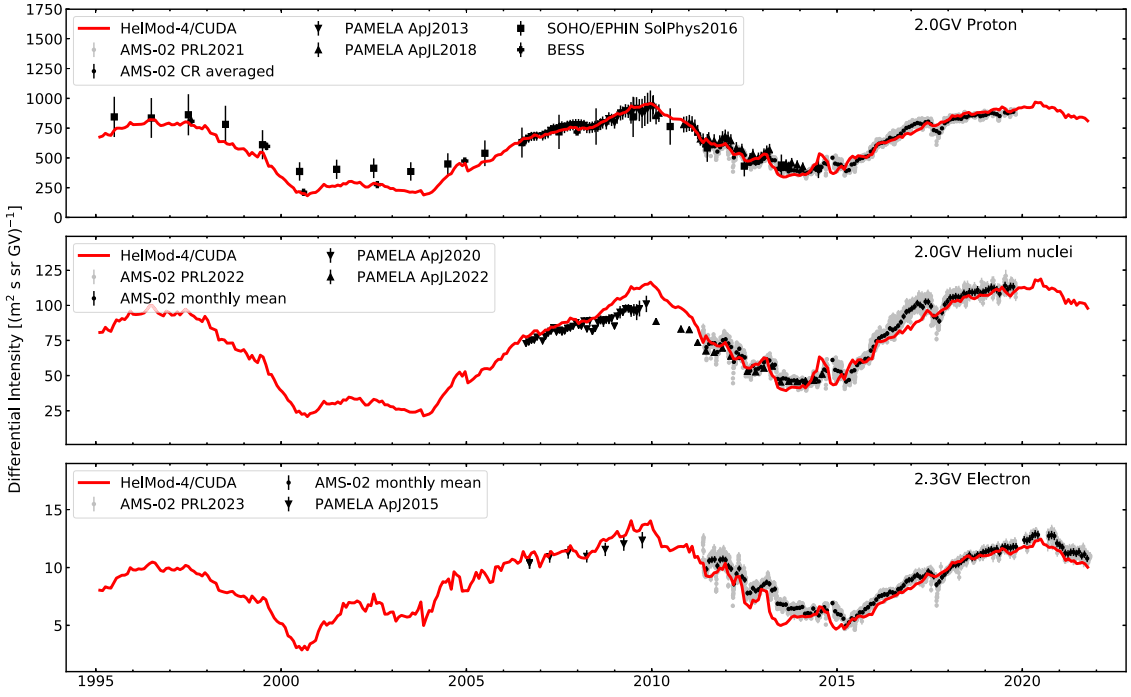

Fig. 8. Solutions of HELMOD-4/CUDA at approximately 2 GV for protons (top panel), helium nuclei (central panel), and electrons (bottom panel) as solid red lines. The gray dots indicate daily fluxes from AMS-02, while the black dots represent their averages in CR time intervals at approximately 2 GV. Additionally, experimental data from EPHIN, BESS, and PAMELA at the nearest rigidity bin are included. For more information, please refer to the text.

Please cite this article as: M. J. Boschini, G. Cavallotto, S. Della Torre et al., Fast and accurate evaluation of deep-space galactic cosmic ray fluxes with HELMOD-4/CUDA, Advances in Space Research, https://doi.org/10.1016/j.asr.2024.04.021

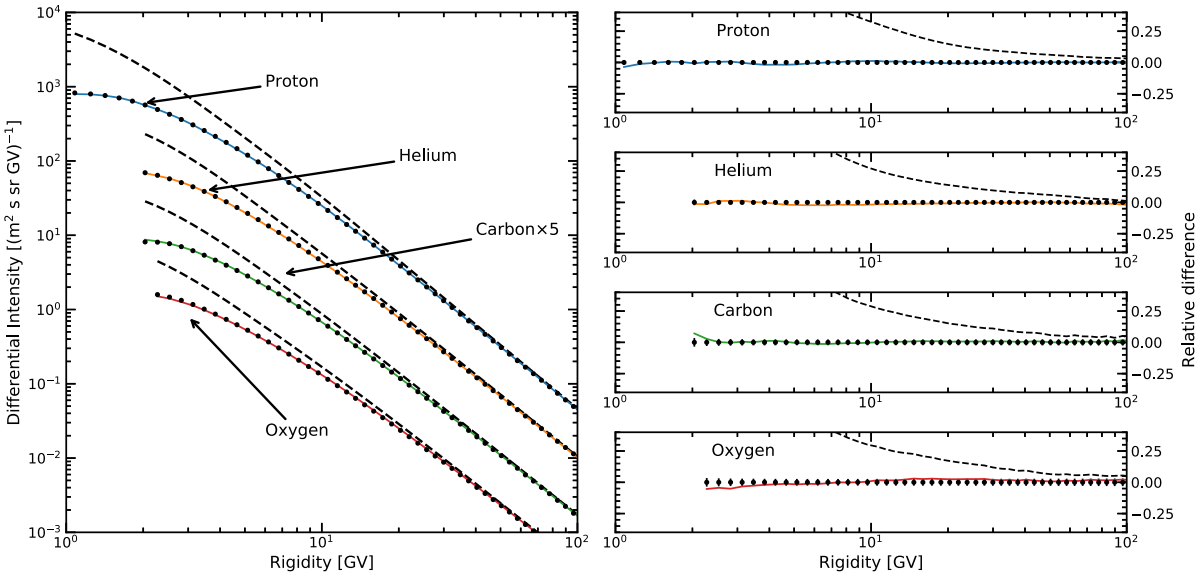

Fig. 9. Modulated spectra observed by AMS-02 (black points), for protons, and nuclei, *i.e.,* helium, carbon and oxygen (Aguilar et al., 2021), are compared with HELMOD-4/CUDA modulated spectra (solid lines). In the figures, the HelMod–GALPROP LISs (dashed black lines) from Boschini et al. (2020b) are also shown. On the left panel, the differential intensities are reported. On the right panel, the relative difference of experimental data with HELMOD-4 simulations and. LISs are shown.

considering AMS-02 data, the agreement falls within the experimental error of a few percent.

Finally, using the parametrization set derived from proton data, we were able to obtain simulated time-integrated fluxes for proton, helium, carbon, and oxygen that agree within the experimental uncertainties, as shown in Fig. 9. The data points in the figure represent AMS-02 measurements over the first seven years of data-taking (from May 2011 to May 2018) as reported by Aguilar et al. (2021). It is worth mentioning that the present results reproduce observed data with a similar degree of accuracy as the previously published results obtained employing the HELMOD-4 model.

4.2. GCR fluxes from the inner to the outer heliosphere and outside the ecliptic plane

Fig. 10 shows the ability of the HELMOD-4/CUDA model to reproduce the radial gradient at larger distances from the Sun. The proton flux measurements are obtained by the Cosmic Ray Subsystem (CRS, Stone et al., 1977) onboard the Voyager 1 and Voyager 2 probes[9], which are flying almost radially towards the outer regions of the heliosphere. The data shown in the figure cover the last 4 solar cycles, from early 1983 up to the Voyager 2 HP crossing at the end of 2019, and are binned over time intervals of three CRs. The same figure also displays the simulation results of HELMOD-4/CUDA. The agreement between the data and simulations is generally good both in the inner heliosphere as well as inside the heliosheath.

In Fig. 11 the proton, helium, and electron normalized counting rates from the Ulysses spacecraft[10] are shown. These rates were observed from December 1990 to June 2009 by the Kiel Electron Telescope (KET) of the Cosmic Ray and Solar Particle Instrument (COSPIN, Simpson et al., 1992). HELMOD-4 normalized fluxes simulated along the spacecraft trajectory are also shown in the figure. Proton and helium counting rates were recorded in two channels that were active in the range of 0.25–2100 MeV/n. The simulated fluxes, on the other hand, were calculated at the representative value of 1.2 GeV (0.5 GeV/n) for proton (helium), corresponding to ∼2 GV for both GCR species. The electron data in the sub-channel E300/K32B were convoluted with the simulations using the geometric factor reported in Rastoin et al. (1996) in the energy range of 0.6–11 GeV. The Ulysses mission includes the beginning of solar cycle 23, corresponding to the minimum of solar activity around August 1996 with positive polarity (analogous to the minimum observed by AMS-02 in December 2019, see Section 2.2), and the beginning of solar cycle 24 with the minimum around December 2008 with negative polarity. The figure shows three fast latitude scans (FLSs), which are marked with gray vertical bands, performed under different conditions of solar activity and IMF polarity. These scans provide valuable insights into the solar modulation mechanisms (*e.g.,* see Heber and

[9] Voyager data are available at https://voyager.gsfc.nasa.gov/spectra.html

[10] Ulysses data have been retrieved from http://ufa.esac.esa.int/ufa/

Please cite this article as: M. J. Boschini, G. Cavallotto, S. Della Torre et al., Fast and accurate evaluation of deep-space galactic cosmic ray fluxes with HELMOD-4/CUDA, Advances in Space Research, https://doi.org/10.1016/j.asr.2024.04.021

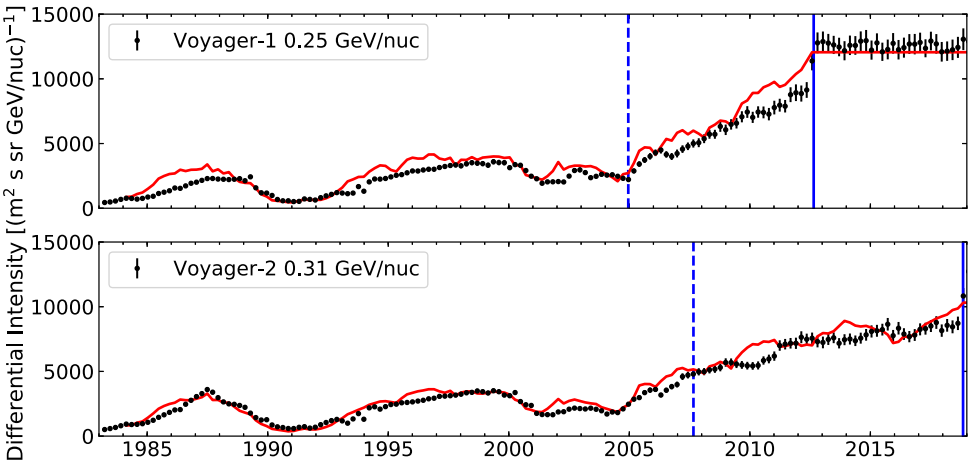

Fig. 10. The black points represent proton flux measurements taken at 0.25 GeV and 0.31 GeV from instruments aboard Voyager 1 and Voyager 2 respectively. The red solid line in the upper and lower panels of the plot shows the modulated spectra from HELMOD-4/CUDA. The Voyager data is sourced from NASA-Voyager (2023). All data points are plotted with both their statistical and systematic uncertainties added in quadrature (see Cummings et al., 2016). The vertical dashed (full) blue line indicates the time of T.S (HP) crossing.

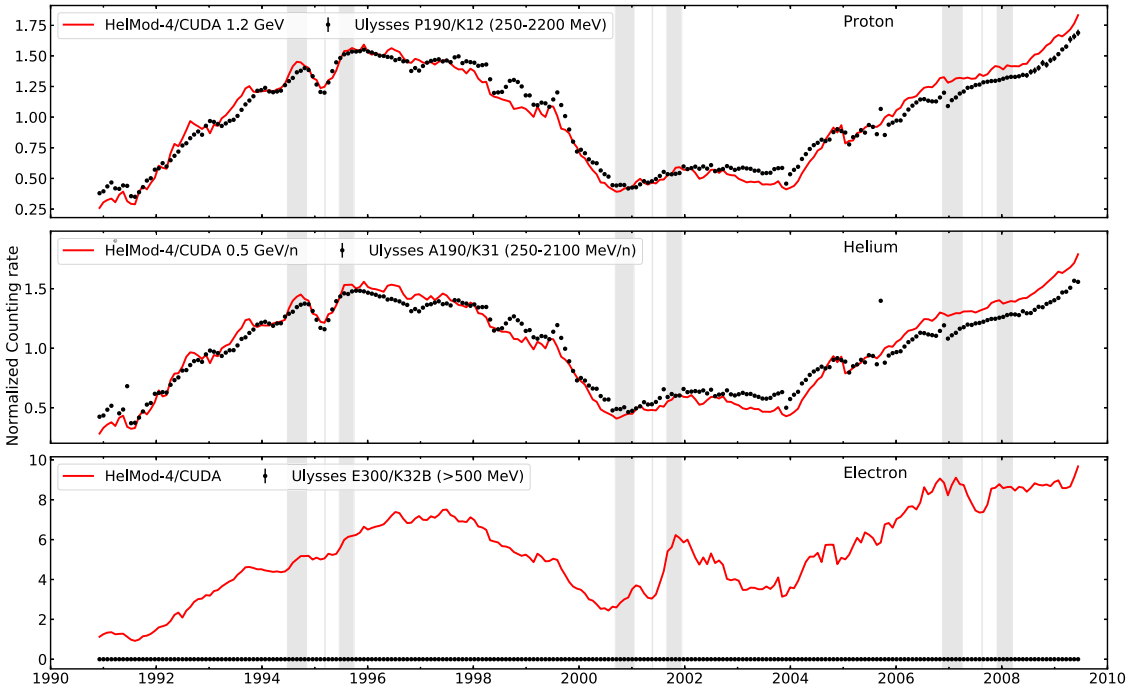

Fig. 11. Counting rates for protons (top panel), helium nuclei (central panel), and electrons (bottom panel) observed by the Ulysses spacecraft (represented by black points) and the simulated fluxes of HELMOD-4/CUDA (represented by red solid lines). The rates are normalized to the average of the period. The gray vertical bands in the figure correspond to the period of the polar passes, *i.e.,* when the spacecraft was above 70° heliographic latitude in either hemisphere. These passes start from the South towards the North pole for each of the three fast latitude scans, with the gray vertical lines indicating the perihelion. For further details, please refer to the text.

Potgieter, 2006). Upon inspection of Fig. 11, it is evident that the HELMOD-4/CUDA simulations and Ulysses rates are in good qualitative agreement.

5. Conclusion

In this work, we presented the HELMOD-4/CUDA model, which includes a better tuning of the descending phase of

Please cite this article as: M. J. Boschini, G. Cavallotto, S. Della Torre et al., Fast and accurate evaluation of deep-space galactic cosmic ray fluxes with HELMOD-4/CUDA, Advances in Space Research, https://doi.org/10.1016/j.asr.2024.04.021

the solar cycle in positive IMF polarity. Both the diffusion coefficient and the drift modelization have been updated, employing the data-driven approach described in Section 2. In this way, we were able to improve the agreement at all rigidities with the latest high-precision data from AMS-02, also during the positive IMF period, as shown in Fig. 2. In general, the updated HELMOD-4 model exhibited a global good agreement also with other available data sets along more than two solar cycles at the Earth location for protons, electrons, and helium nuclei, as shown in Fig. 8. When considering AMS-02 data, the agreement falls within the experimental error of a few percent (*e.g.,* see Fig. 9 for comparison with proton, helium, carbon, and oxygen nuclei integrated-in-time spectra). In addition, simulation results are in qualitatively good agreement with Voyager data in the inner heliosphere as well as inside the heliosheath (see Fig. 10) and with Ulysses counting rates outside the ecliptic plane (see Fig. 11).

We presented the integration algorithm used by HELMOD-4/CUDA and designed to operate on NVIDIA GPUs. The comparison between HELMOD-4 and HELMOD-4/CUDA simulation results shows that the two implementations provide solar-modulated spectra with a similar degree of accuracy in reproducing observed data. Furthermore, the new design of the code is optimized to provide the average modulated spectra even along complicated orbital paths within the heliosphere. We evaluated the improved speed-up by using GPUs with respect to CPUs for several injected statistics. For example, for typical use with ~5'000 *quasi-particle* objects simulated the improved factor is estimated to be ~40 times. The improvements are even bigger for larger statistics. From those tests, it was evident how for a large number of injected particles (i.e. getting lower numerical uncertainties) HELMOD-4/CUDA is significantly faster than HELMOD-4 making feasible the possibility to incorporate HELMOD-4/CUDA within an automatized parameter scan algorithm. These performances, joined with the availability of high-performance GPUs at affordable cost, as well the possibility to install several GPUs on a relatively small cluster make HELMOD-4/CUDA a very competitive product to rapidly assess the space radiation environment due to GCRs along an orbit in the inner heliosphere.

Declaration of Competing Interest

The authors declare that they have no known competing financial interests or personal relationships that could have appeared to influence the work reported in this paper.

Acknowledgments

This work was carried out using the HelMod tool which is currently supported within the framework of space radiation environment activities of ASIF–ASI (Agenzia Spaziale Italiana) Supported Irradiation Facilities–, *e.g.,* ASIF implementation agreements 2017–22-HD.0 ASI-ENEA, 2017–15-HD.0 ASI-INFN, 2021–39-HH.0 ASI-ENEA and ASIF implementation agreement 2021–36-HH.0 involving ASI and Milano-Bicocca University. This work is also supported by ESA (European Space Agency) contract 4000116146/16/NL/HK.

Sunspot data were provided by the World Data Center SILSO, Royal Observatory of Belgium, Brussels. We acknowledge the use of NASA/GSFC's Space Physics Data Facility's OMNIWeb service and OMNI data. We would also like to thank Prof. D. Besozzi and Prof. M. Nobile for their feedback and support throughout the GPU porting process.

Appendix A. Ultra-heavy GCRs contribution to SEEs in deep space

Ultra-heavy GCR ions (UHGCRs) are GCRs that are heavier than nickel, *i.e.,* with a nuclear charge larger than 28. The origin of UHGCRs is a long-standing and important question in the fields of astronomy and astrophysics (see recent reviews in Wiedenbeck et al., 2007; Lingenfelter, 2019; Tatischeff et al., 2021, and references therein). Due to their rarity, measuring their abundance is extremely challenging, and their spectral shape as a function of energy is still unknown. Data mainly consists of ratios of elements or groups of elements in an unspecified energy band. This is due to the limitations of the detectors used to evaluate the abundance, which is typically measured in a range of energies around a few GeV/nucleon.

Abundance measurements of UHGCR are available in the Cosmic-Ray DataBase (CRDB, Maurin et al., 2014; Maurin et al., 2020). Fig. 12 shows their values normalized to the iron abundance plotted against the atomic number Z. The most recent measurements in the Z = 30–40 range are from the SuperTIGER experiment (Rauch et al., 2009; Murphy et al., 2016). However, experiments in the high charge range date back mainly to the late 70s to late 90s of the last century, such as HEAO3 (Binns et al., 1981; Binns et al., 1982; Binns et al., 1983; Binns et al., 1985; Binns et al., 1989), ARIEL6 (Fowler et al., 1987), UHCRE (Domingo et al., 1996; Dutta et al., 2003; Donnelly et al., 2012), and Trek (Westphal et al., 1998; Weaver and Westphal, 2002). Fig. 12 also shows abundances relative to iron for "non-modulated" spectra, listed in Table 2 of the ISO-15390 report (ISO, 2004). This model is recognized by the ECSS[11] guidelines (*e.g.,* see ECSS, 2020) as the standard model to assess the space radiation environment. The Figure also reports ratios of UHGCR fluxes and the iron flux, obtained by the ISO-15390 model implemented in ESA's SPace ENVironment Information System[12] (SPENVIS), at 16.2 GeV/nucleon —at this energy the solar modulation effects can be considered negligible.

[11] European Cooperation for Space Standardization, https://ecss.nl/
[12] https://www.spenvis.oma.be/

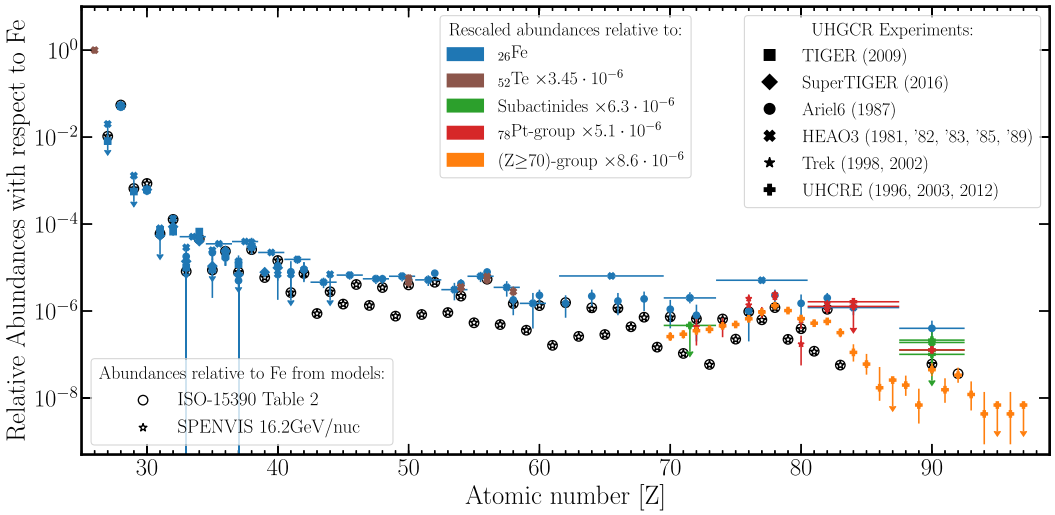

Fig. 12. Relative abundances of GCRs from iron (Z = 26) to berkelium (Z = 97). Open circles represent GCR relative abundances taken from Table 2 of the ISO-15390 model (ISO, 2004). SPENVIS spectra at 16.2 GeV/nucleon are also shown as open stars. These values have been compared with the relative abundance measurements of UHGCRs from various experiments collected in CRDB (Maurin et al., 2020). Different colors refer to abundances measured with respect to the abundance of the ion or the group of ions reported in the respective color legend label; multiplicative factors are used to rescale these values to the Fe abundance. Further details can be found in the text.

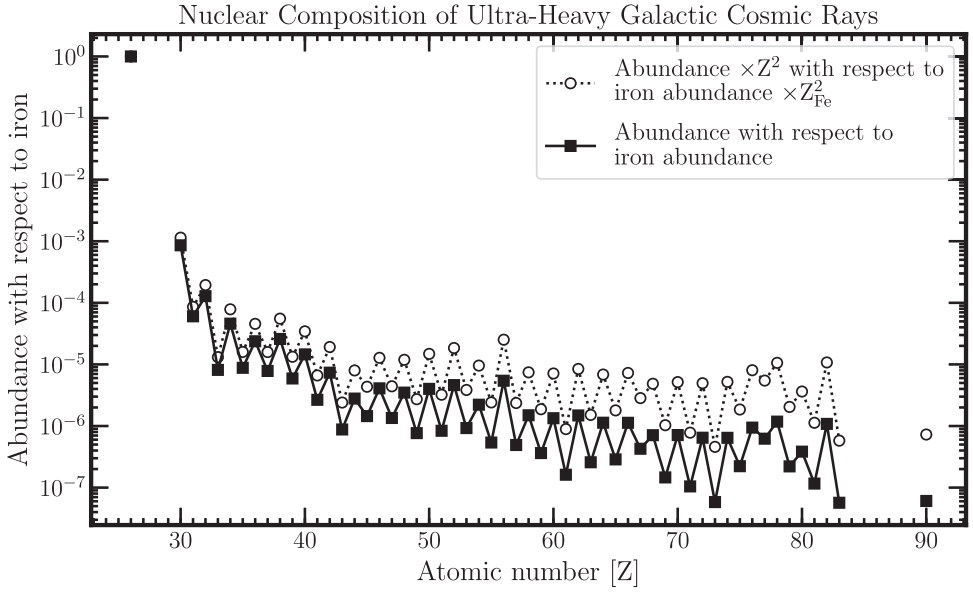

Fig. 13. Relative abundances (black-filled squares) and relative abundances multiplied by Z^2 (open circles) of GCRs at 16.2 GeV/nucleon, normalized to the iron abundance, as a function of the atomic number Z. The plot ranges from copper (Z = 29) to uranium (Z = 92). Please refer to the text for further details.

Fig. 13 displays the ratio of GCR abundances from copper (Z = 29) to uranium (Z = 92) and the iron flux at 16.2 GeV/nucleon, obtained from SPENVIS, as a function of the atomic number Z. Additionally, the relative abundances are also shown multiplied by Z^2, considering that the collision energy-loss in matter at sufficiently high energies is proportional to Z^2. It is observed from the plot that the total amount of energy loss experienced by UHGCRs in the matter is less than 0.5% of the iron energy loss. Therefore, the contribution of UHGCRs to the radiation hazard in space, such as the SEE rate, can be considered negligible.

References

Abdo, A.A., Ackermann, M., Ajello, M., et al., 2009. Measurement of the Cosmic Ray e$^+$+e$^-$ Spectrum from 20GeV to 1TeV with the Fermi Large Area Telescope. Phys. Rev. Lett. 102 (18), 181101. https://doi.org/10.1103/PhysRevLett.102.181101, arXiv:0905.0025.

Abe, K., Fuke, H., Haino, S., et al., 2016. Measurements of cosmic-ray proton and helium spectra from the BESS-Polar Long-duration

Balloon Flights over Antarctica. Astrophys. J. 822, 65. https://doi.org/10.3847/0004-637X/822/2/65, arXiv:1506.01267.

Adriani, O., Barbarino, G.C., Bazilevskaya, G.A., et al., 2013. Time Dependence of the Proton Flux Measured by PAMELA during the 2006 July-2009 December Solar Minimum. ApJ 765 (2), 91. https://doi.org/10.1088/0004-637X/765/2/91, arXiv:1301.4108.

Adriani, O., Barbarino, G.C., Bazilevskaya, G.A. et al., 2015. Time Dependence of the e^- Flux Measured by PAMELA during the July 2006-December 2009 Solar Minimum. ApJ, 810(2), 142. doi:10.1088/0004-637X/810/2/142. arXiv:1512.01079.

Adriani, O., Barbarino, G.C., Bazilevskaya, G.A., et al., 2009. An anomalous positron abundance in cosmic rays with energies 1.5-100GeV. Nature 458, 607–609. https://doi.org/10.1038/nature07942, arXiv:0810.4995.

Adriani, O., Barbarino, G.C., Bazilevskaya, G.A., et al., 2011. PAMELA measurements of cosmic-ray proton and helium spectra. Science 332, 69. https://doi.org/10.1126/science.1199172, arXiv:1103.4055.

Aguilar, M., Ali Cavasonza, L., Alpat, B., et al., 2018a. Observation of fine time structures in the cosmic proton and helium fluxes with the alpha magnetic spectrometer on the International Space Station. Phys. Rev. Lett. 121 (5), 051101. https://doi.org/10.1103/PhysRevLett.121.051101.

Aguilar, M., Ali Cavasonza, L., Ambrosi, G., et al., 2021. The alpha magnetic spectrometer (ams) on the international space station: Part ii – results from the first seven years. Phys. Rep. 894, 1–116. https://doi.org/10.1016/j.physrep.2020.09.003.

Aguilar, M., Ali Cavasonza, L., Ambrosi G., B. et al. (AMS Collaboration) (2018b). Observation of complex time structures in the cosmic-ray electron and positron fluxes with the alpha magnetic spectrometer on the international space station. Phys. Rev. Lett., 121, 051102. URL: https://link.aps.org/doi/10.1103/PhysRevLett.121.051102. doi:10.1103/PhysRevLett.121.051102.

Aguilar, M., Cavasonza, L.A., Ambrosi, G., et al., 2023. Temporal Structures in Electron Spectra and Charge Sign Effects in Galactic Cosmic Rays. Phys. Rev. Lett. 130 (16), 161001. https://doi.org/10.1103/PhysRevLett.130.161001.

Aguilar, M., Cavasonza, L.A., Ambrosi, G., et al., 2021. Periodicities in the Daily Proton Fluxes from 2011 to 2019 Measured by the Alpha Magnetic Spectrometer on the International Space Station from 1 to 100 GV. Phys. Rev. Lett. 127 (27), 271102. https://doi.org/10.1103/PhysRevLett.127.271102.

Aguilar, M., Cavasonza, L.A., Ambrosi, G., et al., 2022. Properties of Daily Helium Fluxes. Phys. Rev. Lett. 128 (23), 231102. https://doi.org/10.1103/PhysRevLett.128.231102.

Alvey, J., Bringmann, T., Kolesova, H., 2023. No room to hide: implications of cosmic-ray upscattering for GeV-scale dark matter. J. High Energy Phys. 2023 (1), 123. https://doi.org/10.1007/JHEP01(2023)123, arXiv:2209.03360.

Askar, T., Shukirgaliyev, B., Lukac, M., et al., 2021. Evaluation of pseudo-random number generation on gpu cards. Computation 9 (12), URL: https://www.mdpi.com/2079-3197/9/12/142.

Bartocci, S., Battiston, R., Burger, W.J., et al., 2020. Galactic Cosmic-Ray Hydrogen Spectra in the 40–250 MeV Range Measured by the High-energy Particle Detector (HEPD) on board the CSES-01 Satellite between 2018 and 2020. ApJ 901 (1), 8. https://doi.org/10.3847/1538-4357/abad3e.

Binns, W.R., Fickle, R.K., Waddington, C.J., et al., 1981. Cosmic-ray abundances of elements with atomic number 26 less than or equal to 40 measured on HEAO 3. ApJ 247, L115–L118. https://doi.org/10.1086/183602.

Binns, W.R., Garrard, T.L., Gibner, P.S., et al., 1989. Abundances of Ultraheavy Elements in the Cosmic Radiation: Results from HEAO 3. ApJ 346, 997. https://doi.org/10.1086/168082.

Binns, W.R., Israel, M.H., Brewster, N.R., et al., 1985. Lead, platinum, and other heavy elements in the primary cosmic radiation - HEAO 3 results. ApJ 297, 111–118. https://doi.org/10.1086/163508.

Binns, W.R., Israel, M.H., Klarmann, J., et al., 1983. Cosmic-ray abundances of Sn, Te, Xe, and BA nuclei measured on HEAO 3. ApJ 267, L93–L96. https://doi.org/10.1086/184010.

Binns, W.R., Israel, M.H., Klarmann, J., et al., 1982. The abundance of the actinides in the cosmic radiation as measured on HEAO 3. ApJ 261, L117–L120. https://doi.org/10.1086/183899.

Bobik, P., Boella, G., Boschini, M.J., et al., 2012. Systematic Investigation of Solar Modulation of Galactic Protons for Solar Cycle 23 Using a Monte Carlo Approach with Particle Drift Effects and Latitudinal Dependence. Astrophys. J. 745, 132. https://doi.org/10.1088/0004-637X/745/2/132.

Bobik, P., Boella, G., Boschini, M.J., et al., 2013. Latitudinal dependence of cosmic rays modulation at 1 au and interplanetary magnetic field polar correction. Advances in Astronomy 2013. https://doi.org/10.1155/2013/793072.

Bobik, P., Boschini, M.J., Della Torre, S., et al., 2016. On the forward-backward-in-time approach for monte carlo solution of parker's transport equation: One-dimensional case. J. Geophys. Res.: Space Phys. 121 (5), 3920–3930. https://doi.org/10.1002/2015JA022237.

Boschini, M., Della Torre, S., Gervasi, M. et al. (2023). Predicting galactic cosmic ray intensities in the heliosphere employing the HelMod-4 model. In Proceedings of 38th International Cosmic Ray Conference — PoS(ICRC2023) (p. 1289). volume 444. doi:10.22323/1.444.1289.

Boschini, M.J., Della Torre, S., Gervasi, M. et al. (2022a). A hint of a low-energy excess in cosmic-ray fluorine. The Astrophysical Journal, 925 (2), 108. URL: https://arxiv.org/abs/2106.01626. doi:10.3847/1538-4357/ac313d. arXiv:2106.01626.

Boschini, M.J., Della Torre, S., Gervasi, M., et al., 2018a. Propagation of cosmic rays in heliosphere: the helmod model. Adv. Space Res. 62 (10), 2859–2879. https://doi.org/10.1016/j.asr.2017.04.017.

Boschini, M.J., Della Torre, S., Gervasi, M., et al., 2019. The helmod model in the works for inner and outer heliosphere: From ams to voyager probes observations. Adv. Space Res. 64 (12), 2459–2476. https://doi.org/10.1016/j.asr.2019.04.007.

Boschini, M.J., Della Torre, S., Gervasi, M., et al., 2022b. Forecasting of cosmic rays intensities with HELMOD Model. Adv. Space Res. 70 (9), 2649–2657. https://doi.org/10.1016/j.asr.2022.01.031.

Boschini, M.J., Della Torre, S., Gervasi, M., et al., 2022c. The transport of galactic cosmic rays in heliosphere: The HELMOD model compared with other commonly employed solar modulation models. Adv. Space Res. 70 (9), 2636–2648. https://doi.org/10.1016/j.asr.2022.03.026.

Boschini, M.J., Della Torre, S., Gervasi, M., et al., 2017. Solution of Heliospheric Propagation: Unveiling the Local Interstellar Spectra of Cosmic-ray Species. ApJ 840, 115. https://doi.org/10.3847/1538-4357/aa6e4f.

Boschini, M.J., Della Torre, S., Gervasi, M., et al., 2018b. Deciphering the local interstellar spectra of primary cosmic-ray species with helmod. Astrophys. J. 858 (1), 61. https://doi.org/10.3847/1538-4357/aabc54.

Boschini, M.J., Della Torre, S., Gervasi, M., et al., 2018c. Helmod in the works: From direct observations to the local interstellar spectrum of cosmic-ray electrons. Astrophys. J. 854 (2), 94. https://doi.org/10.3847/1538-4357/aaa75e.

Boschini, M.J., Della Torre, S., Gervasi, M., et al., 2020a. Deciphering the local interstellar spectra of secondary nuclei with the galprop/helmod framework and a hint for primary lithium in cosmic rays. Astrophys. J. 889 (2), 167. https://doi.org/10.3847/1538-4357/ab64f1.

Boschini, M.J., Della Torre, S., Gervasi, M., et al., 2020b. Inference of the local interstellar spectra of cosmic-ray nuclei $z < 28$ with the GalProp-HelMod framework. Astrophys. J. Supplement 250 (2), 27. https://doi.org/10.3847/1538-4365/aba901.

Boschini, M.J., Della Torre, S., Gervasi, M., et al., 2021. The discovery of a low-energy excess in cosmic-ray iron: Evidence of the past supernova activity in the local bubble. Astrophys J 913 (1), 5. https://doi.org/10.3847/1538-4357/abf11c.

Boschini, M.J., Torre, S.D., Gervasi, M. et al. (2022d). Spectra of Cosmic-Ray Sodium and Aluminum and Unexpected Aluminum Excess. ApJ, 933(2), 147. doi:10.3847/1538-4357/ac7443. arXiv:2202.09928.

Please cite this article as: M. J. Boschini, G. Cavallotto, S. Della Torre et al., Fast and accurate evaluation of deep-space galactic cosmic ray fluxes with HELMOD-4/CUDA, Advances in Space Research, https://doi.org/10.1016/j.asr.2024.04.021

Bottino, A., Donato, F., Fornengo, N., et al., 1998. Which fraction of the measured cosmic-ray antiprotons might be due to neutralino annihilation in the galactic halo?. Phys. Rev. D. 58 (12) 123503. https://doi.org/10.1103/PhysRevD.58.123503, arXiv:astro-ph/9804137.

Cernuda, I. (2011). Anisotropies in the cosmic-ray electron spectrum: a way to discriminate between exotic and astrophysical sources? In S. Giani, C. Leroy, & P.G. Rancoita (Eds.), Cosmic Rays for Particle and Astroparticle Physics (pp. 513–518). doi:10.1142/9789814329033_0063.

Chang, J., Adams, J.H., Ahn, H.S., et al., 2008. An excess of cosmic ray electrons at energies of 300–800GeV. Nature 456, 362–365. https://doi.org/10.1038/nature07477.

Cheng, J., Grossman, M., McKercher, T., 2014. Professional CUDA C Programming, 1st ed. Wrox Press Ltd., GBR.

Cirelli, M., Cline, J.M., 2010. Can multistate dark matter annihilation explain the high-energy cosmic ray lepton anomalies? Phys. Rev. D. 82 (2), 023503. https://doi.org/10.1103/PhysRevD.82.023503, arXiv:1005.1779.

Clette, F., Svalgaard, L., Cliver, E.W. et al. (2015). The new Sunspot and Group Numbers: a full recalibration. In IAU General Assembly (p. 2249591). volume 29.

Corti, C., Potgieter, M.S., Bindi, V., et al., 2019. Numerical Modeling of Galactic Cosmic-Ray Proton and Helium Observed by AMS-02 during the Solar Maximum of Solar Cycle 24. ApJ 871 (2), 253. https://doi.org/10.3847/1538-4357/aafac4, arXiv:1810.09640.

Cummings, A.C., Stone, E.C., Heikkila, B.C., et al., 2016. Galactinc cosmic rays in the local interstellar medium: Voyager 1 observations and model results. Astrophys J 831 (1), 18. https://doi.org/10.3847/0004-637x/831/1/18.

De Simone, N., Di Felice, V., Gieseler, J., et al., 2011. Latitudinal and radial gradients of galactic cosmic ray protons in the inner heliosphere - PAMELA and Ulysses observations. Astrophysics and Space Sciences Transactions 7, 425–434. https://doi.org/10.5194/astra-7-425-2011.

Della Torre, S., Bobik, P., Boschini, M.J., et al., 2012. Effects of solar modulation on the cosmic ray positron fraction. Adv. Space Res. 49, 1587–1592. https://doi.org/10.1016/j.asr.2012.02.017.

Della Torre, S., Cavallotto, G., Besozzi, D. et al. (2023). Advantages of GPU-accelerated approach for solving the Parker equation in the heliosphere. In Proceedings of 38th International Cosmic Ray Conference — PoS(ICRC2023) (p. 1290). volume 444. doi:10.22323/1.444.1290.

Della Torre, S., Gervasi, M., Rancoita, P.G., et al., 2015. Pulsar wind nebulae as a source of the observed electron and positron excess at high energy: The case of vela-x. Journal of High Energy Astrophysics 8, 27–34. https://doi.org/10.1016/j.jheap.2015.08.001, arXiv:1508.01457.

Domingo, C., Font, J., Baixeras, C., et al., 1996. Source abundances of ultra heavy elements derived from UHCRE measurements. Radiat. Meas. 26 (6), 825–832. https://doi.org/10.1016/S1350-4487(96)00090-X.

Donnelly, J., Thompson, A., O'Sullivan, D., et al., 2012. Actinide and Ultra-Heavy Abundances in the Local Galactic Cosmic Rays: An Analysis of the Results from the LDEF Ultra-Heavy Cosmic-Ray Experiment. ApJ 747 (1), 40. https://doi.org/10.1088/0004-637X/747/1/40.

Dunzlaff, P., Strauss, R.D., Potgieter, M.S., 2015. Solving Parker's transport equation with stochastic differential equations on GPUs. Comput. Phys. Commun. 192, 156–165. https://doi.org/10.1016/j.cpc.2015.03.008.

Dutta, A., Batra, V., Biswas, S., 2003. Abundance of actinides in cosmic radiation. Radiat. Meas. 36 (1–6), 287–290. https://doi.org/10.1016/S1350-4487(03)00137-9.

ECSS (2020). Space Environment. Technical Report ECSS-E-ST-10-04C Rev. 1 European Cooperation for Space Standardization, ESA. URL: https://ecss.nl/standard/ecss-e-st-10-04c-rev-1-space-environment-15-june-2020/.

Effenberger, F., Fichtner, H., Scherer, K., et al., 2012. Anisotropic diffusion of Galactic cosmic ray protons and their steady-state azimuthal distribution. A&A 547, A120. https://doi.org/10.1051/0004-6361/201220203, arXiv:1210.1423.

Engelbrecht, N.E., Effenberger, F., Florinski, V., et al., 2022. Theory of Cosmic Ray Transport in the Heliosphere. Space Sci. Rev. 218 (4), 33. https://doi.org/10.1007/s11214-022-00896-1.

Engelmann, J.J., Ferrando, P., Soutoul, A., et al., 1990. Charge composition and energy spectra of cosmic-ray nuclei for elements from Be to Ni - Results from HEAO-3-C2. A&A 233, 96–111, URL: https://ui.adsabs.harvard.edu/abs/1990A&A...233...96E.

Ferrando, P., Raviart, A., Haasbroek, L.J., et al., 1996. Latitude variations of ≈7MeV and >300MeV cosmic ray electron fluxes in the heliosphere: ULYSSES COSPIN/KET results and implications. Astron. Astrophys. 316, 528–537, URL: http://adsabs.harvard.edu/abs/1996A%26A...316.528F.

Florinski, V., Pogorelov, N.V., 2009. Four-dimensional Transport of Galactic Cosmic Rays in the Outer Heliosphere and Heliosheath. Astrophys. J. 701, 642–651. https://doi.org/10.1088/0004-637X/701/1/642.

Fowler, P.H., Walker, R.N.F., Masheder, M.R.W., et al., 1987. Ariel 6 Measurements of the Fluxes of Ultra-heavy Cosmic Rays. ApJ 314, 739. https://doi.org/10.1086/165101.

Gardiner, C., 1985. Handbook of stochastic methods: for physics, chemistry and natural sciences. Springer, Berlin, Heidelberg.

George, J.S., Lave, K.A., Wiedenbeck, M.E., et al., 2009. Elemental Composition and Energy Spectra of Galactic Cosmic Rays During Solar Cycle 23. ApJ 698 (2), 1666–1681. https://doi.org/10.1088/0004-637X/698/2/1666.

Gieseler, J., Heber, B., 2016. Spatial gradients of GCR protons in the inner heliosphere derived from Ulysses COSPIN/KET and PAMELA measurements. Astron. and Astrophys. 589, A32. https://doi.org/10.1051/0004-6361/201527972, arXiv:1602.00533.

Golge, S. (2016). NASA galactic cosmic radiation environment model: Badhwar-O'Neill (2014). In Proceedings of The 34th International Cosmic Ray Conference — PoS(ICRC2015) (p. 180). volume 236. doi:10.22323/1.236.0180.

Haino, S., Sanuki, T., Abe, K., et al., 2004. Measurements of primary and atmospheric cosmic-ray spectra with the BESS-TeV spectrometer. Phys. Lett. B 594, 35–46. https://doi.org/10.1016/j.physletb.2004.05.019, arXiv:astro-ph/0403704.

Hattingh, M., Burger, R.A., 1995. A new simulated wavy neutral sheet drift model. Adv. Space Res. 16 (9), 213–216. https://doi.org/10.1016/0273-1177(95)00337-E.

Heber, B., Droege, W., Ferrando, P., et al., 1996. Spatial variation of >40MeV/n nuclei fluxes observed during the ULYSSES rapid latitude scan. Astron. Astrophys. 316, 538–546, URL: http://adsabs.harvard.edu/abs/1996A%26A...316.538H.

Heber, B., Gieseler, J., Dunzlaff, P., et al., 2008. Latitudinal Gradients of Galactic Cosmic Rays during the 2007 Solar Minimum. Astrophys. J. 689, 1443–1447. https://doi.org/10.1086/592596.

Heber, B., Potgieter, M.S., 2006. Cosmic Rays at High Heliolatitudes. Space Sci. Rev. 127 (1–4), 117–194. https://doi.org/10.1007/s11214-006-9085-y.

Higham, D.J., 2001. An Algorithmic Introduction to Numerical Simulation of Stochastic Differential Equations. SIAM Review 43, 525–546. https://doi.org/10.1137/S0036144500378302.

Ibarra, A., Tran, D., & Weniger, C. (2010). Decaying dark matter in light of the PAMELA and Fermi LAT data. J. Cosmol. Astropart. P., 1, 009. doi:10.1088/1475-7516/2010/01/009. arXiv:0906.1571.

ISO (2004). Space Environment (Natural and Artificial) - Galactic Cosmic Ray Model. Standard International Organization for Standardization Geneva, CH. URL: https://www.iso.org/standard/37095.html.

Jokipii, J.R., Thomas, B., 1981. Effects of drift on the transport of cosmic rays. IV - Modulation by a wavy interplanetary current sheet. ApJ 243, 1115–1122. https://doi.org/10.1086/158675.

Klöden, P.E., Platen, E., 1999. Numerical Solution of Stochastic Differential Equations. Springer, Berlin, Heidelberg.

Kolesnyk, Y.L., Shakhov, B.A., Bobik, P., et al., 2020. An exact solution of cosmic ray modulation problem in a stationary composite

Please cite this article as: M. J. Boschini, G. Cavallotto, S. Della Torre et al., Fast and accurate evaluation of deep-space galactic cosmic ray fluxes with HELMOD-4/CUDA, Advances in Space Research, https://doi.org/10.1016/j.asr.2024.04.021

heliosphere model. MNRAS 491 (4), 5826–5842. https://doi.org/10.1093/mnras/stz3343.

Kopp, A., Büsching, I., Strauss, R.D., et al., 2012. A stochastic differential equation code for multidimensional Fokker-Planck type problems. Comput. Phys. Commun. 183, 530–542. https://doi.org/10.1016/j.cpc.2011.11.014.

Krimigis, S.M., Decker, R.B., Roelof, E.C., et al., 2019. Energetic charged particle measurements from Voyager 2 at the heliopause and beyond. Nature Astronomy 3, 997–1006. https://doi.org/10.1038/s41550-019-0927-4.

Kroese, D.P., Taimre, T., Botev, Z.I., 2011. Handbook of Monte Carlo methods. Wiley, New York City, United States.

Kühl, P., Dresing, N., Heber, B., et al., 2017. Solar Energetic Particle Events with Protons Above 500 MeV Between 1995 and 2015 Measured with SOHO/EPHIN. Sol. Phys. 292 (1), 10. https://doi.org/10.1007/s11207-016-1033-8, arXiv:1611.03289.

Lingenfelter, R.E., 2019. The Origin of Cosmic Rays: How Their Composition Defines Their Sources and Sites and the Processes of Their Mixing, Injection, and Acceleration. ApJS 245 (2), 30. https://doi.org/10.3847/1538-4365/ab4b58, arXiv:1903.06330.

Marcelli, N., Boezio, M., Lenni, A., et al., 2020. Time Dependence of the Flux of Helium Nuclei in Cosmic Rays Measured by the PAMELA Experiment between 2006 July and 2009 December. ApJ 893 (2), 145. https://doi.org/10.3847/1538-4357/ab80c2, arXiv:2005.08524.

Marcelli, N., Boezio, M., Lenni, A., et al., 2022. Helium Fluxes Measured by the PAMELA Experiment from the Minimum to the Maximum Solar Activity for Solar Cycle 24. ApJ 925 (2), L24. https://doi.org/10.3847/2041-8213/ac4787, arXiv:2201.01045.

Martucci, M., Munini, R., Boezio, M., et al., 2018. Proton Fluxes Measured by the PAMELA Experiment from the Minimum to the Maximum Solar Activity for Solar Cycle 24. ApJ 854 (1), L2. https://doi.org/10.3847/2041-8213/aaa9b2, arXiv:1801.07112.

Maurin, D., Dembinski, H.P., Gonzalez, J., et al., 2020. Cosmic-Ray Database Update: Ultra-High Energy, Ultra-Heavy, and Antinuclei Cosmic-Ray Data (CRDB v4.0). Universe 6 (8), 102. https://doi.org/10.3390/universe6080102, arXiv:2005.14663.

Maurin, D., Melot, F., Taillet, R., 2014. A database of charged cosmic rays. A&A 569, A32. https://doi.org/10.1051/0004-6361/201321344, arXiv:1302.5525.

McDonald, F.B., Ferrando, P., Heber, B., et al., 1997. A comparative study of cosmic ray radial and latitudinal gradients in the inner and outer heliosphere. J. Geophys. Res. 102, 4643–4652. https://doi.org/10.1029/96JA03673.

Mertsch, P., & Sarkar, S. (2011). The 'PAMELA anomaly' indicates a nearby cosmic ray accelerator. In S. Giani, C. Leroy, & P.G. Rancoita (Eds.), Cosmic Rays for Particle and Astroparticle Physics (pp. 535–543). doi:10.1142/9789814329033_0066. arXiv:1108.1753.

Moiseev, A., Yoshimura, K., Ueda, I., et al., 1997. Cosmic-Ray Antiproton Flux in the Energy Range from 200 to 600 MeV. ApJ 474 (1), 479–489. https://doi.org/10.1086/303463.

Moloto, K.D., Engelbrecht, N.E., Strauss, R.D., et al., 2019. Numerical integration of stochastic differential equations: A parallel cosmic ray modulation implementation on Africa's fastest computer. Adv. Space Res. 63 (1), 626–639. https://doi.org/10.1016/j.asr.2018.08.048.

Murphy, R.P., Sasaki, M., Binns, W.R., et al., 2016. Galactic Cosmic Ray Origins and OB Associations: Evidence from SuperTIGER Observations of Elements $_{26}$Fe through $_{40}$Zr. ApJ 831 (2), 148. https://doi.org/10.3847/0004-637X/831/2/148, arXiv:1608.08183.

Mykhailenko, V., Bobik, P., 2022. Statistical Error for Cosmic Rays Modulation Evaluated by SDE Backward in Time Method for 1D Model. Fluidika 7 (2), 46. https://doi.org/10.3390/fluids7020046.

NASA-Voyager (2023). Online database https://voyager.gsfc.nasa.gov/flux.html.

Ngobeni, M.D., Aslam, O.P.M., Bisschoff, D., et al., 2020. The 3d numerical modeling of the solar modulation of galactic protons and helium nuclei related to observations by pamela between 2006 and 2009. Astrophys Space Sci 365 (182). https://doi.org/10.1007/s10509-020-03896-1.

Nndanganeni, R.R., & Potgieter, M.S. (2016). The energy range of drift effects in the solar modulation of cosmic ray electrons. Advances in Space Research, 58(3), 453–463. URL: https://www.sciencedirect.com/science/article/pii/S0273117716301557. doi: 10.1016/j.asr.2016.04.020.

Parker, E.N., 1963. Interplanetary dynamical processes. Interscience Publishers, New York.

Parker, E.N., 1965. The passage of energetic charged particles through interplanetary space. Plan. Space Sci. 13, 9–49. https://doi.org/10.1016/0032-0633(65)90131-5.

Peter, J.S., Schuemann, J., Held, K.D., et al., 2022. Nano-scale simulation of neuronal damage by galactic cosmic rays. Physics in Medicine and Biology 67 (23), 235001. https://doi.org/10.1088/1361-6560/ac95f4, arXiv:2202.07547.

Picozza, P., Galper, A.M., Castellini, G., et al., 2007. PAMELA A payload for antimatter matter exploration and light-nuclei astrophysics. Astropart. Phys. 27 (4), 296–315. https://doi.org/10.1016/j.astropartphys.2006.12.002, arXiv:astro-ph/0608697.

Potgieter, M.S., Moraal, H., 1985. A drift model for the modulation of galactic cosmic rays. Astrophys. J. 294 (part 1), 425–440. https://doi.org/10.1086/163309.

Rahmanian, S., Slaba, T.C., Braby, L.A., et al., 2023. Galactic cosmic ray environment predictions for the NASA BioSentinel mission. Life Sciences and Space Research 38, 19–28. https://doi.org/10.1016/j.lssr.2023.05.001.

Rankin, J.S., Bindi, V., Bykov, A.M., et al., 2022a. Galactic Cosmic Rays Throughout the Heliosphere and in the Very Local Interstellar Medium. Space Sci. Rev. 218 (5), 42. https://doi.org/10.1007/s11214-022-00912-4.

Rankin, J.S., McComas, D.J., Leske, R.A. et al. (2022b). Anomalous Cosmic-Ray Oxygen Observations into 0.1 au. ApJ, 925(1), 9. doi:10.3847/1538-4357/ac348f. arXiv:2110.03601.

Rastoin, C., Ferrando, P., Raviart, A., et al., 1996. Time and space variations of the Galactic cosmic ray electron spectrum in the 3-D heliosphere explored by Ulysses. A&A 307, 981–995, URL: https://ui.adsabs.harvard.edu/abs/1996A&A...307.981R.

Rauch, B.F., Link, J.T., Lodders, K., et al., 2009. Cosmic Ray origin in OB Associations and Preferential Acceleration of Refractory Elements: Evidence from Abundances of Elements $_{26}$Fe through $_{34}$Se. ApJ 697 (2), 2083–2088. https://doi.org/10.1088/0004-637X/697/2/2083, arXiv:0906.2021.

Richardson, J.D., Belcher, J.W., Garcia-Galindo, P., et al., 2019. Voyager 2 plasma observations of the heliopause and interstellar medium. Nature Astronomy 3, 1019–1023. https://doi.org/10.1038/s41550-019-0929-2.

Romero, J., Bisson, M., Fatica, M. et al. (2020). High performance implementations of the 2d ising model on gpus. Computer Physics Communications, 256, 107473. URL: https://www.sciencedirect.com/science/article/pii/S0010465520302228. doi: 10.1016/j.cpc.2020.107473.

Rozza, D., Della torre, S., Gervasi, M. et al. (2016). Vela-X as main contributor to the electron and positron spectra at energy above 100 GeV. In Proceedings of The 34th International Cosmic Ray Conference — PoS(ICRC2015) (p. 501). volume 236. doi:10.22323/1.236.0501.

Salati, P. (2011). Charged Cosmic Rays from Dark Matter. In S. Giani, C. Leroy, & P.G. Rancoita (Eds.), Cosmic Rays for Particle and Astroparticle Physics (pp. 613–625). doi:10.1142/9789814329033_0076.

Salmon, J.K., Moraes, M.A., Dror, R.O. et al. (2011). Parallel random numbers: As easy as 1, 2, 3. In Proceedings of 2011 International Conference for High Performance Computing, Networking, Storage and Analysis number 16 in SC '11 (p. 12). New York, NY, USA: Association for Computing Machinery. URL: https://doi.org/10.1145/2063384.2063405. doi:10.1145/2063384.2063405.

Please cite this article as: M. J. Boschini, G. Cavallotto, S. Della Torre et al., Fast and accurate evaluation of deep-space galactic cosmic ray fluxes with HELMOD-4/CUDA, Advances in Space Research, https://doi.org/10.1016/j.asr.2024.04.021

Samwel, S.W., El-Aziz, E.A., Garrett, H.B., et al., 2019. Space radiation impact on smallsats during maximum and minimum solar activity. Adv. Space Res. 64 (1), 239–251. https://doi.org/10.1016/j.asr.2019.03.025.

Shen, Z.N., Qin, G., Zuo, P., et al., 2019. Modulation of Galactic Cosmic Rays from Helium to Nickel in the Inner Heliosphere. ApJ 887 (2), 132. https://doi.org/10.3847/1538-4357/ab5520.

Shikaze, Y., Haino, S., Abe, K., et al., 2007. Measurements of 0.2 20 GeV/n cosmic-ray proton and helium spectra from 1997 through 2002 with the BESS spectrometer. Astropart. Phys. 28, 154–167. https://doi.org/10.1016/j.astropartphys.2007.05.001, arXiv:astro-ph/0611388.

SILSO World Data Center (1965-2022). The International Sunspot Number. International Sunspot Number Monthly Bulletin and online catalogue,. URL: https://www.sidc.be/SILSO/home.

Simpson, J.A., 1996. Ulysses cosmic-ray investigations extending from the south to the north polar regions of the Sun and heliosphere. Nuovo Cimento C Geophysics Space Physics C 19, 935–943. https://doi.org/10.1007/BF02508134.

Simpson, J.A., Anglin, J.D., Balogh, A., et al., 1992. The ULYSSES Cosmic Ray and Solar Particle Investigation. Astronomy and Astrophysics Supplement Series 92, 365–399, URL: http://adsabs.harvard.edu/abs/1992A%26AS...92.365S.

Solanik, M., Bobik, P., & Genci, J. (2021). Cosmic rays modulation in heliosphere models on GPU. In Proceedings of 37th International Cosmic Ray Conference — PoS(ICRC2021) (p. 1320). volume 395. doi:10.22323/1.395.1320.

Solanik, M., Bobik, P., Genci, J., 2023. Geliosphere - parallel cpu and gpu based models of cosmic ray modulation in the heliosphere. Comput. Phys. Commun. 291, 108847. https://doi.org/10.1016/j.cpc.2023.108847.

Stone, E.C., Cummings, A.C., McDonald, F.B., et al., 2005. Voyager 1 Explores the Termination Shock Region and the Heliosheath Beyond. Science 309, 2017–2020. https://doi.org/10.1126/science.1117684.

Stone, E.C., Vogt, R.E., McDonald, F.B., et al., 1977. Cosmic ray investigation for the Voyager missions; energetic particle studies in the outer heliosphere—And beyond. Space Sci. Rev. 21 (3), 355–376. https://doi.org/10.1007/BF00211546.

Strauss, R.D., Potgieter, M.S., Büsching, I., et al., 2011. Modeling the Modulation of Galactic and Jovian Electrons by Stochastic Processes. Astrophys. J. 735, 83. https://doi.org/10.1088/0004-637X/735/2/83.

Strauss, R.D.T., Effenberger, F., 2017. A Hitch-hiker's Guide to Stochastic Differential Equations. Solution Methods for Energetic Particle Transport in Space Physics and Astrophysics. Space Sci. Rev. 212 (1–2), 151–192. https://doi.org/10.1007/s11214-017-0351-y, arXiv:1703.06192.

Tatischeff, V., Raymond, J.C., Duprat, J., et al., 2021. The origin of Galactic cosmic rays as revealed by their composition. MNRAS 508 (1), 1321–1345. https://doi.org/10.1093/mnras/stab2533, arXiv:2106.15581.

Usoskin, I.G., Alanko-Huotari, K., Kovaltsov, G.A., et al., 2005. Heliospheric modulation of cosmic rays: Monthly reconstruction for 1951–2004. Journal of Geophysical Research (Space Physics) 110 (A9), A12108. https://doi.org/10.1029/2005JA011250.

Usoskin, I.G., Bazilevskaya, G.A., Kovaltsov, G.A., 2011. Solar modulation parameter for cosmic rays since 1936 reconstructed from ground-based neutron monitors and ionization chambers. Journal of Geophysical Research: Space Physics 116 (A2), A02104. https://doi.org/10.1029/2010JA016105.

Vogt, A., Engelbrecht, N.E., Strauss, R.D., et al., 2020. The residence-time of Jovian electrons in the inner heliosphere. A&A 642, A170. https://doi.org/10.1051/0004-6361/201936897, arXiv:2006.16768.

Weaver, B.A., Westphal, A.J., 2002. Extended Analysis of the Trek Ultraheavy Collector. ApJ 569 (1), 493–500. https://doi.org/10.1086/339265.

Webber, W.R., McDonald, F.B., 2013. Recent Voyager 1 data indicate that on 25 August 2012 at a distance of 121.7 AU from the Sun, sudden and unprecedented intensity changes were observed in anomalous and galactic cosmic rays. Geophys. Res. Lett. 40, 1665–1668. https://doi.org/10.1002/grl.50383.

Weniger, C., 2011. Gamma-ray anisotropies from decaying dark matter. In: Cosmic Rays for Particle and Astroparticle Physics. WORLD SCIENTIFIC, pp. 632–640. https://doi.org/10.1142/9789814329033_0078.

Westphal, A.J., Price, P.B., Weaver, B.A., et al., 1998. Evidence against stellar chromospheric origin of Galactic cosmic rays. Nature 396 (6706), 50–52. https://doi.org/10.1038/23887.

Wiedenbeck, M.E., Binns, W.R., Cummings, A.C., et al., 2007. An Overview of the Origin of Galactic Cosmic Rays as Inferred from Observations of Heavy Ion Composition and Spectra. Space Sci. Rev. 130 (1–4), 415–429. https://doi.org/10.1007/s11214-007-9198-y.

Zhang, M., 1999. A Markov Stochastic Process Theory of Cosmic-Ray Modulation. Astrophys. J. 513, 409–420. https://doi.org/10.1086/306857.

Zhao, L.L., Qin, G., Zhang, M., et al., 2014. Modulation of galactic cosmic rays during the unusual solar minimum between cycles 23 and 24. J. Geophys. Res. (Space Phys.) 119 (3), 1493–1506. https://doi.org/10.1002/2013JA019550, arXiv:1310.7076.

Please cite this article as: M. J. Boschini, G. Cavallotto, S. Della Torre et al., Fast and accurate evaluation of deep-space galactic cosmic ray fluxes with HELMOD-4/CUDA, Advances in Space Research, https://doi.org/10.1016/j.asr.2024.04.021